

ENHANCED MULTI-RESOLUTION ANALYSIS FOR MULTI-DIMENSIONAL DATA UTILIZING LINE FILTERING TECHNIQUES

MATTHEW J. PICKLO*†‡ AND JENNIFER K. RYAN*†§

Abstract. In this article we introduce Line Smoothness-Increasing Accuracy-Conserving Multi-Resolution Analysis (LSIAC-MRA). This is a procedure for exploiting convolution kernel post-processors for obtaining more accurate multi-resolution analysis (MRA) in multiple dimensions. This filtering-projection tool allows for the transition of data between different resolutions while simultaneously decreasing errors in the fine grid approximation. It specifically allows for defining detail multi-wavelet coefficients when translating coarse data onto finer meshes. These coefficients are usually not defined in such cases. We show how to analytically evaluate the resulting convolutions and express the filtered approximation in a new basis. This allows for combining the filtering procedure with projection operators that allow for efficient computational implementation of this scale transition procedure. Further, this procedure can be applied to piecewise constant approximations to functions, contrary to the theory of SIAC filters. We demonstrate the effectiveness of this technique in two- and three-dimensions.

Key words. Discontinuous Galerkin, post-processing, SIAC filtering, Line filtering, accuracy enhancement, error reduction, Multi-Resolution Analysis

AMS subject classifications. 65M60

1. Introduction. Approximating multi-scale phenomena accurately and efficiently has its significance illustrated in such areas as turbulence modeling and kinetics among many other applications. Of considerable importance is the ability to match data on a coarse grid with that on a fine grid. Multi-resolution analysis (MRA) is one technique that is useful in accomplishing such a task [1, 9]. MRA expresses the approximation in terms of averages and differences, with the differences being the details between a fine grid approximation and coarse grid approximation. The MRA approximation usually starts at the finest grid and moves to a coarser grid. The reverse is a challenging procedure as the difference coefficients no longer exist. In this paper, we introduce a procedure which allows for approximating the difference coefficients and allowing for error reduction when moving to a finer grid. To do so, we introduce Line Smoothness-Increasing Accuracy-Conserving multi-resolution analysis (LSIAC-MRA). As the name suggests, it relies on the Line SIAC filter found in [8] that is an improvement over the tensor-product SIAC filters [4, 20, 7, 11] and was used for MRA in [16]. We present the necessary operators and algorithms to accomplish this task as well as demonstrating its effectiveness on two- and three-dimensional functions. Aside from demonstrating that LSIAC-MRA can reduce the errors with mesh refinement, we show that it is also effective on piecewise constant approximations, contradicting previous speculation that the SIAC filter was not effective on such data.

Multi-resolution Analysis (MRA) is a useful technique for moving data between successive mesh refinements. Alpert, Belykin, and collaborators introduced this technique in [1, 9]. It is based on the idea that an approximation can be represented as scaling functions, which are typically the approximation basis, and wavelets. The scaling functions give the averages of the approximation over a coarse grid and the wavelet information contains the information necessary to move to a finer grid. Mathematically, the expression is the following:

$$(1.1) \quad \underbrace{u_h^f(x, t)}_{\text{fine grid approximation}} = \underbrace{u_h^c(x, t)}_{\text{coarse grid information}} + \underbrace{\sum_{j=1}^N \sum_{k=0}^p d_{k,j}^N(t) \psi_{k,j}^c(x)}_{\text{details necessary to move to a finer grid}} .$$

The basis functions for the multi-wavelet space is given by Alpert's multiwavelets $\psi_{k,j}^c(x)$. The multi-wavelets associated to the piecewise orthonormal Legendre approximation are given in [1]. In this expression, both the scaling functions and wavelets are piecewise polynomials of degree p .

In creating this variant of Nyström reconstruction [15], we utilize the LSIAC filter [8] for multi-dimensional data. Nyström reconstruction also uses convolution for accurate reconstructions. For

*Applied Mathematics and Statistics, Colorado School of Mines, Golden, CO 80401, USA.

†Research supported by Air Force Office of Scientific Research (AFOSR), Computational Mathematics Program (Program Manager: Dr. Fariba Fahroo), under grant numbers FA9550-20-1-0166 and FA9550-19-S-0003.

‡Email: mpicklo@mymail.mines.edu

§Corresponding Author. Email: jkryan@mines.edu

27 LSIAC-MRA, it allows for reducing the computational cost of the multi-dimensional filtering operation by
 28 introducing a one-dimensional support for the convolution kernel.

29 Pairing Smoothness-Increasing Accuracy-Conserving (SIAC) post-processing with the multi-resolution
 30 analysis presented in [1, 9] is natural. Although SIAC has broad applicability, it has mostly been developed
 31 for discontinuous Galerkin (DG) methods, which rely on a piecewise polynomial approximation basis. An
 32 initial introduction to this pairing in one-dimension can be found in [16]. However, the multi-dimensional
 33 equivalent is challenging as discussed in Section 4. Therefore in order to get to this stage we discuss the
 34 necessary background in multi-resolution analysis (Section 2.2), Line SIAC (Section 2.3) before introducing
 35 LSIAC-MRA as a means to approximate difference coefficients. Demonstration of the effectiveness of this
 36 technique can be found in Section 5.

37 **2. Background.** In the following sections we introduce the necessary background for understanding
 38 the enhanced multi-resolution analysis for multi-dimensions. To better illustrate the ideas, we begin with a
 39 discussion of the one-dimensional ideas discussed in [16].

40 **2.1. Input Data Format.** For ease of discussion, we will assume our data is given in a modal format.
 41 This generalizes to the nodal format by simply assuming that the approximation basis is the Lagrange
 42 polynomial basis. Therefore, we describe the procedure for constructing projected approximations for higher
 43 dimensional quadrilateral and hexahedral meshes under consideration. In the following, we introduce the
 44 necessary definitions.

45 For a given function $u(\mathbf{x})$, we wish to construct a piecewise-polynomial approximation $u_h(\mathbf{x})$. To
 46 do so, we utilize the following notation. A multi-index $\alpha = (\alpha_1, \dots, \alpha_n)$ is an n -tuple of non-negative
 47 integers. Define $|\alpha| = \sum_{i=1}^n \alpha_i$, and $\partial^\alpha = \partial^{\alpha_1} \dots \partial^{\alpha_n}$, where $\partial^{\alpha_i} = \frac{\partial}{\partial x^{\alpha_i}}$. Let $\mathbf{x} = (x_1, \dots, x_d)$. Consider a d -
 48 dimensional rectangular domain and its partition into N^d d -dimensional rectangular elements: $\Omega = \bigcup_{\beta \in \mathbb{B}} K_\beta$,
 49 where the indexing set is given by

$$\mathbb{B} = \{\beta \in \mathbb{N}^d : \|\beta\|_{\ell^\infty} \leq N\}.$$

50 Borrowing from a discontinuous Galerkin type approximation, we define an approximation space over our
 51 partition that will contain piecewise-polynomials in d variables up to a given degree p :

$$V_h^p = \{v \in L^2 : v \in \mathbb{P}^p(K_\beta), \beta \in \mathbb{B}\}.$$

52 We assume that our piecewise-polynomial approximation to $u(\mathbf{x})$ is obtained via L^2 -projection, that is on
 53 a given element K_β , we write

$$u_h(\mathbf{x}) \Big|_{K_\beta} = \sum_{\|\alpha\|_{\ell^\infty} \leq p} u_\alpha^\beta \phi_\alpha^\beta(\mathbf{x}),$$

54 where $\{\phi_\alpha^\beta\}_{\|\alpha\|_{\ell^\infty} \leq p}$ is a basis for our approximation space on K_β , and the coefficients u_α^β are computed by
 55 projecting the given $u(\mathbf{x})$ onto the piecewise polynomials basis:

$$\langle u, \phi_\alpha \rangle_{K_\beta} = \langle u_h, \phi_\alpha \rangle_{K_\beta}, \quad \|\alpha\|_{\ell^\infty} \leq p, \beta \in \mathbb{B}.$$

56 **2.2. Multi-Resolution Analysis.** Multi-resolution analysis (MRA) allows for a framework in which to
 57 analyze modal approximations under scale transition. Specifically, MRA views approximations as belonging
 58 to a hierarchy of nested approximation spaces, where transition between scales is simply the addition or
 59 removal of finer-detail basis functions called multi-wavelets. To better express the utility of this setting as
 60 it relates to our modal projections, we provide a brief summary of MRA as detailed in [16]. More in depth
 61 introductions to multi-resolution analyses generated by scaling functions can be found in [3, 5, 1, 2]. For
 62 ease of presentation, the one-dimensional case is given.

63 Consider a nested sequence of approximation spaces

$$V_0^p \subset V_1^p \subset \dots \subset V_n^p \subset \dots,$$

64 where each approximation space is given by

$$V_n^p = \{v : v \in \mathbb{P}^p(I_j^n), j = 0, \dots, 2^n - 1\},$$

65 with

$$I_j^n = (-1 + 2^{-n+1}j, -1 + 2^{-n+1}(j+1)), \quad j = 0, \dots, 2^n - 1.$$

66 We denote by $\{\phi_k(x)\}_{k=0}^p$ the orthonormal basis on the coarsest mesh consisting of one element, $n = 0$.
 67 These basis functions are called *scaling functions*, owing to fact that the systematic manner in which our
 68 approximation space and the underlying mesh is refined allows for construction of bases for any V_n^p simply
 69 by scaling and translating the coarse mesh basis functions. For example, the basis functions for V_n^p can be
 70 chosen as

$$\phi_{k,j}^n = 2^{n/2} \phi_k(2^n(x+1) - 2j-1), \quad k = 0, \dots, p, \quad j = 0, \dots, 2^n - 1.$$

71 We can then express our global modal approximation on a mesh of $N = 2^n$ elements as

$$(2.1) \quad u_h^N(x) = 2^{-n/2} \sum_{j=0}^{2^n-1} \sum_{k=0}^p u_j^k \phi_{k,j}^n(x).$$

72 The intermediary information which is required to advance from a coarse approximation space V_n^p to a finer
 73 approximation space V_{n+1}^p is contained within the wavelet space W_n^p which is defined as the orthogonal
 74 compliment of V_n^p in V_{n+1}^p :

$$V_{n+1}^p = V_n^p \oplus W_n^p, \quad W_n^p \subset V_{n+1}^p, \quad W_n^p \perp V_n^p.$$

75 Inductively, this hierarchy allows the expression of the fine-mesh approximation space as the direct sum of
 76 the coarsest mesh approximation spaces and the intermediary wavelet spaces:

$$V_n^p = V_0^p \oplus W_0^p \oplus W_1^p \oplus \dots \oplus W_{n-1}^p.$$

77 Alternatively, this means our fine mesh approximations are simply coarse mesh approximations plus details
 78 contained within these wavelet spaces. We denote the basis functions for W_n^p by $\psi_{k,j}^n$, $k = 0, \dots, p$, $j =$
 79 $1, \dots, 2^n - 1$. These functions are known as multi-wavelets. Decomposing our approximation in an analogous
 80 manner to our approximation spaces, we have the that our fine mesh approximation is just the sum of a
 81 coarse mesh approximation (on a mesh consisting of N elements) and multi-wavelets:

$$u_h^f(x) = u_h^N(x) + \sum_{j=0}^{2^n-1} \sum_{k=0}^p d_{k,j}^n \psi_{k,j}^n(x).$$

82 An illustration of this idea in two-dimensions is given in Figure 2.1. As a result, we see that one manner of
 83 obtaining fine-mesh approximations is to take a coarse-mesh approximation and add a linear combination of
 84 multi-wavelets, where the detail coefficient $d_{k,j}^n$ serve as the weights. The difficulty is that when only given
 85 approximation information on a coarse grid, we do not have these finer details. SIAC-MRA [16] enables a way
 86 of approximating detail coefficients $\hat{d}_{k,j}^n$ when only coarse mesh information is given. Or, as an alternative
 87 for moving approximations from a coarse mesh to a fine mesh.

88 **2.3. Multi-dimensional SIAC Filter.** The Smoothness-Increasing Accuracy-Conserving (SIAC)
 89 post-processor is a convolution kernel originally designed to enable superconvergence in finite element
 90 numerical methods [4, 20]. They have since been extended for derivatives, boundaries and nonlinear
 91 hyperbolic equations in [17, 19, 21, 10, 18, 12] as well as mesh adaptivity in [6]. The SIAC filter has
 92 been generalized for application to higher dimensional data using two methods [20, 8]: the first is a tensor
 93 product SIAC filter, whereby a convolution kernel is constructed by taking the tensor product of multiple
 94 one-dimensional SIAC kernels; the second is to construct a Line SIAC filter (L-SIAC), which is simply a one-
 95 dimensional SIAC kernel that has been rotated to align with a non-Cartesian axis. Both of these techniques
 96 rely on understanding the one-dimensional kernel.

97 In one dimension, the SIAC filtered approximation is defined by

$$(2.2) \quad u_h^*(x) = K_H \star u_h = \int_{-\infty}^{\infty} K_H^{(r+1,\ell)}(x-y) u_h(y) dy,$$

98 where the convolution kernel $K_H(x) = \frac{1}{H} K\left(\frac{x}{H}\right)$ is a scaled linear combination of $r+1$ central B-splines of
 99 order ℓ :

$$K^{(r+1,\ell)}(t) = \sum_{\gamma=-r/2}^{r/2} c_{\gamma} B^{(\ell)}(t + \gamma).$$

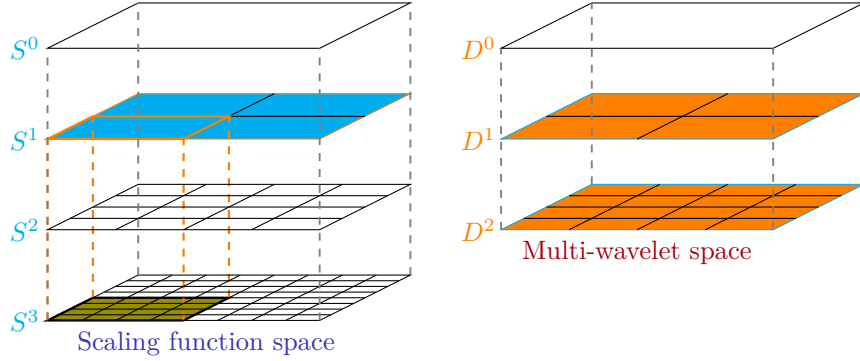


Fig. 2.1: Illustration of the two-dimensional multi-wavelet idea. The approximation at the finest level, S^3 , can be represented as the approximation from the S^1 scaling function space plus the multi-wavelet coefficients from wavelet spaces D^1 and D^2 .

100 The coefficients c_γ are chosen so that the kernel reproduces polynomials up to degree r :

$$K^{(r+1,\ell)} \star x^k = x^k \text{ for } k = 0, \dots, r,$$

while the central B-splines are piecewise polynomials defined recursively via the relation

$$\begin{aligned} B^{(1)} &= \chi_{[-1/2, 1/2]} \\ B^{(n+1)} &= B^{(n)} \star B^{(1)} \\ &= \frac{1}{n} \left[(n/2 + t) B^{(n)}(t + 1/2) + (n/2 - t) B^{(n)}(t - 1/2) \right]. \end{aligned}$$

101 Central B-splines are used in the kernel construction as they provide finite support to the kernel,
102 while allowing derivatives of the kernel to be expressed as divided differences. This later property and
103 the preservation of moments condition are important in deriving the error estimates [4, 10, 13, 14]. The
104 kernel is scaled by a parameter H typically set as the uniform element width h . To enable superconvergence
105 in DG approximations we require $r = 2p$ and $\ell = p + 1$. This allows for our filtered approximation to obtain
106 $\mathcal{O}(h^{2p+1})$ errors in the L^2 -norm and L^∞ -norm for linear hyperbolic equations.

107 In 2D the Line SIAC filter is given by

$$(2.3) \quad u_h^*(\mathbf{x}) = \int_{\Gamma} K_{\Gamma, H}^{(r+1,\ell)}(t) u_h(t) dt,$$

108 where

$$\Gamma(t) = (x_1, x_2) + t(\cos(\theta), \sin(\theta)),$$

and

$$(2.4) \quad K_{\Gamma, H}^{(r+1,\ell)}(t) = \sum_{\gamma=-r/2}^{r/2} c_\gamma B_H^{(\ell)}(t - \gamma) = \frac{1}{H} \sum_{\gamma=-r/2}^{r/2} c_\gamma B^{(\ell)}\left(\frac{t}{H} - \gamma\right).$$

The angle of rotation θ and the scaling parameter H are selected to be

$$(2.5) \quad \theta = \tan^{-1}\left(\frac{h_{x_2}}{h_{x_1}}\right), \quad H = h_{x_1} \cos(\theta) + h_{x_2} \sin(\theta).$$

109 In this article we choose the uniform mesh diagonal, $\theta = \pi/4$, and subsequently $H = \sqrt{2}h_{x_1} = \sqrt{2}h_{x_2}$. In
110 higher dimensions we simply need to choose a new orientation and scaling factor. In three-dimensional space,
111 the filtered approximation is given similarly where the line Γ parameterized by t is given by

$$(2.6) \quad \Gamma(t) = \mathbf{x} + t(\cos(\theta) \sin(\phi), \sin(\theta) \sin(\phi), \cos(\phi)) = \mathbf{x} + t\mathbf{v},$$

112 with θ, ϕ being the orientation of the line in spherical coordinates. Because our approximation lies on a
 113 uniform three-dimensional mesh, the line filter will be aligned with one of the four diagonals connecting
 114 antipodal points of the cubic element. Hence, we choose $H = \sqrt{3}h$, where h is the uniform mesh spacing,
 115 and $\theta = \pi/4, \phi = \tan^{-1}(\sqrt{2})$. This results in the direction vector $\mathbf{v} = \frac{1}{\sqrt{3}}(1, 1, 1)$.

116 The utility of the L-SIAC filter is its ability to filter higher-dimensional data without increasing the
 117 dimensionality of the kernel support. This makes it an attractive alternative to the tensor product filter
 118 when evaluating the convolution via quadrature sums. For example, in 2D for a quadratic approximation
 119 it can reduce the number of quadrature sums from 4000 to ten(!). Additionally, the error constant in the
 120 error estimate is reduced for the filtered solution. We consider the L-SIAC filter specifically because of its
 121 reduced and rotated kernel support in this context. The ability to manipulate the kernel orientation and
 122 dimensionality is anticipated to be useful in generalizing to triangulations due to the nature of the multi-variate
 123 basis functions.

124 **3. Multi-dimensional Line SIAC-MRA.** In this section, we introduce Line SIAC for more accurate
 125 multi-resolution analysis. This procedure allows us to obtain detail coefficients for moving information to
 126 successively finer grids. These detail coefficients are obtained for a uniform mesh by setting $r = 2p$ and $\ell = 1$
 127 in the LSIAC filter (Equation (2.4)). This ensures enough moments in the underlying data are respected
 128 as well as ensuring over-smoothing does not occur. For this choice of parameters, the filter coefficients are
 129 given by the equation

$$(3.1) \quad \sum_{\gamma=-p}^p c_{\gamma} \frac{1}{m+1} \left[\left(\frac{1}{2} - \gamma \right)^{m+1} + \left(\frac{1}{2} + \gamma \right)^{m+1} \right] = \begin{cases} 1, & m = 0 \\ 0, & m = 1, \dots, 2p \end{cases}.$$

130 As presented in [16], the one-dimensional convolution, (2.2), can be analytically calculated and thereby
 131 allows for expressing our filtered approximation in a new basis. As a result of the ordering of mesh and
 132 kernel breaks, we have a piecewise definition for the filtered approximation itself:

$$u_h^*(x) = \begin{cases} \sum_{m=0}^{p+1} d_m^j \chi_L^m(\zeta), & \zeta \in (-1, 0) \\ \sum_{m=0}^{p+1} \tilde{d}_m^j \chi_R^m(\zeta), & \zeta \in (0, 1) \end{cases},$$

133 for each element. Here $\zeta = \xi_j(x)$ represents a local element mapping. The basis functions used in this article
 134 and associated coefficients are given in the supplementary materials. Denote the fine-mesh approximation
 135 by $u_h^f = \mathcal{P}_{h/2} u_h^*$, where $\mathcal{P}_{h/2}$ represents the projection operator onto an approximation space $V_{h/2}^p$ consisting
 136 of $2N$ elements. To obtain the fine-mesh modal coefficients in the ansatz $u_h^f(x)|_{I_n} = \sum_{k=0}^p u_k^n \phi_k^j(x)$, $n =$
 137 $1, \dots, 2N$ we require

$$\langle u_h^f, \phi_m^j \rangle_{I_n} = \langle u_h^*, \phi_m^j \rangle_{I_n}, \quad m = 0, \dots, p.$$

138 Hence, depending on the parity of n we obtain

$$u_k^n = \begin{cases} \frac{4}{\Delta x} \sum_{m=0}^{p+1} d_m^{1/2(n+1)} \langle \chi_L^m, \phi_m^n \rangle_{I_n}, & n \text{ odd} \\ \frac{4}{\Delta x} \sum_{m=0}^{p+1} \tilde{d}_m^{1/2(n)} \langle \chi_R^m, \phi_m^n \rangle_{I_n}, & n \text{ even} \end{cases}.$$

139 Having determined our fine-mesh approximation $u_h^f = \mathcal{P}_{h/2} u_h^*$, we can isolate the multi-wavelet
 140 component simply by subtraction of the coarse-approximation in Equation (2.1):

$$\sum_{j=0}^{2^{n-1}-1} \sum_{k=0}^p \hat{d}_{k,j}^n \psi_{k,j}^n(x) = \mathcal{P}_{h/2} u_h^* - u_h.$$

141 These alternative multi-wavelet coefficients provide an improvement to our approximation by introducing a
 142 definition for the multi-wavelet coefficients. This allows for effectively transitioning the approximation onto
 143 a finer mesh. Additionally, it only requires coarse mesh data to be constructed. This differs significantly
 144 from traditional MRA where multi-wavelet coefficients are intrinsically dependent upon initial function u ,
 145 and so we cannot construct multi-wavelet coefficients for improving our approximation if only coarse modal
 146 data is available.

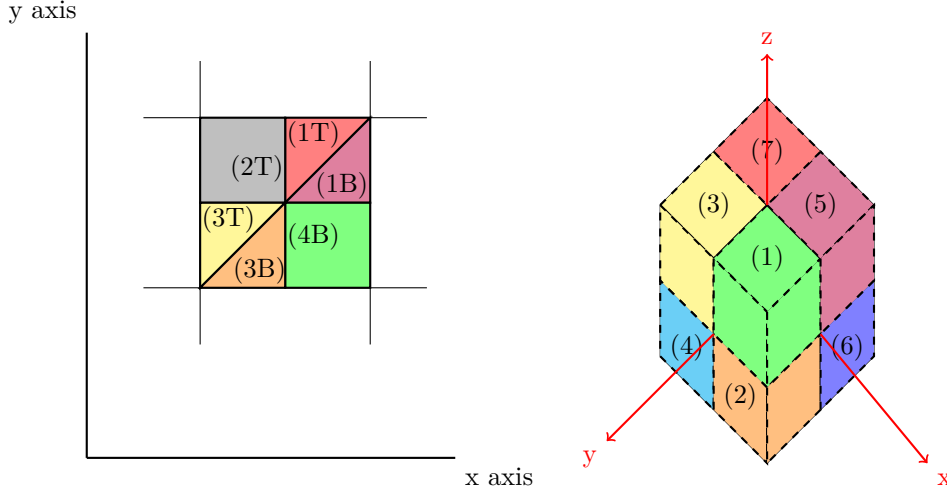


Fig. 3.1: Partition of domain for both 2D L-SIAC (left) and the octant numbering scheme in 3D (right).

147 Knowing the form of the filtered approximation, we can map the filtered approximation coefficients to
 148 the fine-mesh modes simply by application of a projection operator. Furthermore, knowing the forms of the
 149 filtered approximation allows us to discretize this procedure and construct projection operators to perform
 150 this scale transition. This will be discussed further in the implementation Section 4.

151 As demonstrated in [16], repeated application of the filtering-projection procedure results in increasingly
 152 better approximations. It should be noted that SIAC-MRA is mesh-dependent in that our ability to simplify
 153 the convolution is intrinsically linked to patterns in the mesh construction. In this paper we consider uniform
 154 quadrilateral and hexahedral meshes, but further generalizations to arbitrary triangulations will result in new
 155 basis functions. We now generalize this procedure to higher dimensional spaces and introduce LSIAC-MRA.

156 In a manner analogous to the one-dimensional case [16], we can take advantage of the simplicity of
 157 the kernel's B-spline components and the predictability of the element boundaries to analytically evaluate
 158 the convolutions given by Equation (2.3). Following this procedure, and letting $\zeta_x = \xi_i(x)$, $\zeta_y = \xi_j(y)$,
 159 and $\zeta_z = \xi_k(z)$ denote the mapping of our filtering point to the reference element, we obtain the following
 160 expressions for our filtered approximations:

161 For the two-dimensional Line SIAC, the filtered approximation can be written as

$$(3.2) \quad u_h^*(x, y) = \sum_{P=\{L,M,R\}} \sum_{m=0}^p \sum_{r=0}^p a_{m,r}^{S,P,i,j} \chi_{S,P}^{m,r}(\zeta_x, \zeta_y),$$

162 where (x, y) belongs to region S of element (i, j) . These regions are delineated in Figure (3.1). Analogously,
 163 the three-dimensional LSIAC filtered approximation can be written as

$$(3.3) \quad u_h^*(x, y, z) = \sum_{P=\{L,LM,RM,R\}} \sum_{m=0}^p \sum_{r=0}^p \sum_{\ell=0}^p a_{m,r,\ell}^{S,P,i,j,k} \chi_{S,P}^{m,r,\ell}(\zeta_x, \zeta_y, \zeta_z),$$

164 where (x, y, z) belongs to region S of element (i, j, k) . A description of the aforementioned regions and an
 165 associated classification scheme are provided in the supplementary materials.

166 An illustration of the different domains for the new approximation space is given in Figure 3.1. In two
 167 dimensions, the the LSIAC implementation requires 6 quadrature domains per element. In three dimension,
 168 there are 24 quadrature domains per element. Note that for the L-SIAC filters, more complicated integrals
 169 of shifted Legendre Polynomials are produced. Though the reduced dimension of the L-SIAC kernel support
 170 means less information is needed to compute the a coefficients, the integrand is no longer separable which
 171 leads to more complicated functions in the expansion. All the χ functions and their associated coefficients are
 172 detailed in the supplementary materials. Much the same as in one dimension, we can project these filtered

173 approximations onto the finer mesh, and thereby construct fine-mesh approximations. The only difference
 174 is that we are now projecting onto either the quadrant or octants of reference element in two and three
 175 dimensions respectively. In the L-SIAC case this requires us to account for the piecewise definition of the
 176 filtered approximations and split up projections according to the associated domains of definition.

177 In what follows we demonstrate the performance of LSIAC-MRA . Because $\psi^{(1)}(x) = \chi_{[-1/2,1/2]}(x)$, we
 178 were able to analytically evaluate the convolution for the L-SIAC kernel by easily accounting for mesh and
 179 kernel breaks. This enabled us to obtain a closed form expression for the filtered approximation expressed
 180 in a new basis. This allows for our improved multi-resolution analysis technique.

181 **4. Implementation.** For simplicity we describe the implementation in the two-dimensional case. We
 182 begin with a description of the transition operators and then a discussion of the computational algorithm.

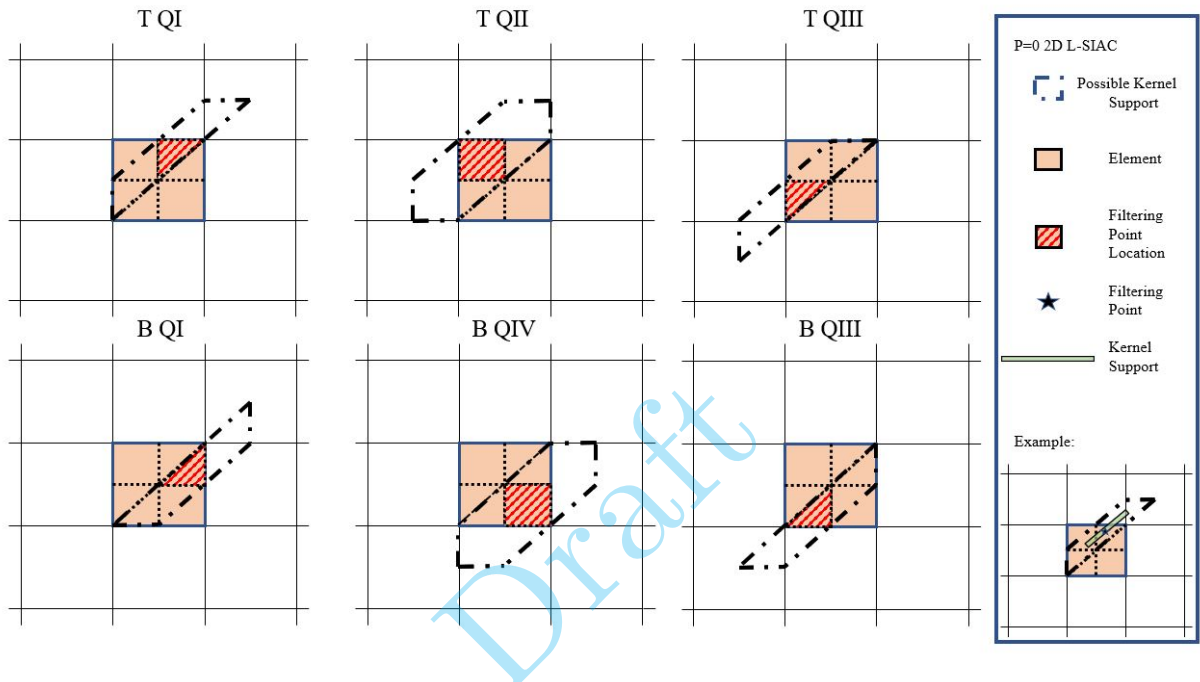


Fig. 4.1: 2D depiction of the varying element overlap of the L-SIAC kernel resulting in varying filtered approximation forms.

183 **4.1. Transition Operators.** We have one transition operator per quadrant in 2D and one per octant
 184 in 3D. In our discrete setting these transition matrices are the composition of the discrete filtering and
 185 projection matrices $T = \mathcal{P}_{h/2}K_H$. It is important to note that, as displayed in Figure 3.1, the sequencing
 186 of mesh and kernel breaks, and the elements within the kernel's support varies from region to region (see
 187 Figure (4.1)). To compute our refined approximation, we project our filtered approximation onto that mesh.
 188 In the L-SIAC case we must sum the projections over the two triangular regions composing quadrants I
 189 and III. Given the fine-mesh modal approximation, the modal coefficients can be obtained by simple matrix
 190 multiplications of the coarse mesh coefficients. This leads to the construction of transition matrices, linear
 191 transformations that map the coarse-mesh modal coefficients to their refined fine-mesh counterparts. In the
 192 following we outline that procedure.

Constructing the transition matrices is easier if modal coefficients are grouped by element. Denote the $(N^2(p+1))^2 \times 1$ vector of modal coefficients by

$$\vec{u} = [\vec{u}^1 \quad | \quad \dots \quad | \quad \vec{u}^N]^T,$$

where

$$\vec{u}^j = [\vec{u}^{1,j} \dots \vec{u}^{N,j}]^T,$$

$$\vec{u}^{i,j} = [\vec{u}_0^{i,j} \quad | \quad \dots \quad | \quad \vec{u}_p^{i,j}]^T,$$

and

$$\vec{u}_{ky}^{i,j} = [u_{0,ky}^{i,j} \quad | \quad \dots \quad | \quad u_{p,ky}^{i,j}]^T.$$

4.1.1. Sifting Matrices. All of the coefficients fit the form $a_{m,r}^{i,j}(q_x, q_y) = \sum_{\gamma=-p}^p c_\gamma u_{kx,ky}^{i+\gamma+q_x, j+\gamma+q_y}$ for $q_x, q_y \in \{-1, 0, 1\}$. To compute these coefficients a selection matrix, $\mathcal{S}^{i,j}$, is first constructed. Presuming periodic boundary conditions, this matrix will select all modes relevant to computing coefficients on that element. It is constructed by composition of sub-matrices. Define the $(2p+3)N(p+1)^2 \times N^2(p+1)^2$ matrix S^j by

$$S^j = \begin{bmatrix} \ddots & & \vdots & & \ddots \\ \dots & \omega_j(m, r) \mathbb{I}_{N(p+1)^2 \times N(p+1)^2} & \dots & & \dots \\ \ddots & & \vdots & & \ddots \end{bmatrix}$$

where

$$\omega_j(m, r) = \begin{cases} 1, & j \neq N \text{ \& } p+2-m+r = j \pmod{N} \\ 1, & j = N \text{ \& } p+2-m+r = j \text{ or } 0 \\ 0, & \text{else} \end{cases},$$

for $m = 1 : (2p+3)$ and $r = 1 : N$. This matrix selects the relevant j -coordinates:

$$S^j \vec{u} = [u^{j-(p+1)} \dots u^{j+(p+1)}]^T.$$

Next, construct an $(2p+3)(p+1)^2 \times N(p+1)^2$ matrix \tilde{S}^i to select the relevant i -coordinates from within each vector. Define

$$\tilde{S}^i = \begin{bmatrix} \ddots & & \vdots & & \ddots \\ \dots & \delta_i(m, r) \mathbb{I}_{(p+1)^2 \times (p+1)^2} & \dots & & \dots \\ \ddots & & \vdots & & \ddots \end{bmatrix}$$

for $m = 1 : (2p+3)$ and $r = 1 : N$. We have that

$$\tilde{S}^i u^j = [u^{i-(p+1),j} \dots u^{i+(p+1),j}]^T.$$

Hence, defining $\mathcal{S}^{i,j}$ to be the $(2p+3)^2(p+1)^2 \times N^2(p+1)^2$ matrix given by

$$\mathcal{S}^{i,j} = \begin{bmatrix} \tilde{S}^i & 0 \\ \ddots & \ddots \\ 0 & \tilde{S}^i \end{bmatrix} S^j,$$

where there are $(2p+3)$ \tilde{S}^i matrices on the diagonal, we have

$$\mathcal{S}^{i,j} u = \left[[u^{i-(p+1),j-(p+1)} \dots u^{i+(p+1),j-(p+1)}] \quad \dots \quad [u^{i-(p+1),j+(p+1)} \dots u^{i+(p+1),j+(p+1)}] \right]^T = \tilde{u}^{i,j}$$

which contains modal information from the $(2p+3)^2$ elements around element (i, j) .

4.1.2. Coefficient Matrices. Now to construct matrices for computing the appropriate coefficients as determined by the (q_x, q_y) index. First, construct an intermediary matrix C^{q_x, q_y} whose function is to select the elements from $\tilde{u}^{i,j}$ which falls within the support of the line integral. Define the $(2p+1)(p+1)^2 \times (2p+3)(p+1)^2$ matrix C^{q_x} by

$$C^{q_x} = \begin{bmatrix} \delta_{-1,q_x} \mathbb{I} & \delta_{0,q_x} \mathbb{I} & \delta_{1,q_x} \mathbb{I} & & 0 \\ & \ddots & \ddots & \ddots & \\ 0 & & \delta_{-1,q_x} \mathbb{I} & \delta_{0,q_x} \mathbb{I} & \delta_{1,q_x} \mathbb{I} \end{bmatrix},$$

194 where δ is the Kronecker delta and \mathbb{I} is the $(p+1)^2 \times (p+1)^2$ identity matrix. This matrix has the effect
 195 of selecting the relevant i -coordinates. Then define the $(2p+1)^2(p+1)^2 \times (2p+3)^2(p+1)^2$ matrix \mathcal{C}^{q_x, q_y}
 196 by

$$\mathcal{C}^{q_x, q_y} = \begin{bmatrix} \delta_{-1, q_y} C^{q_x} & \delta_{0, q_y} C^{q_x} & \delta_{1, q_y} C^{q_x} & & 0 \\ & \ddots & \ddots & \ddots & \\ 0 & & \delta_{-1, q_y} C^{q_x} & \delta_{0, q_y} C^{q_x} & \delta_{1, q_y} C^{q_x} \end{bmatrix},$$

This concatenated matrix has the effect:

$$\mathcal{C}^{q_x, q_y} \tilde{u}^{i, j} = \tilde{u}_{q_x, q_y}^{i, j} = [u^{i-(p-q_x), j-(p-q_y)}, \dots, u^{i+(p+q_x), j+(p+q_y)}]^T,.$$

Thus it selects exactly the modes used in computing the sum $a_{m,r}^{i,j}(q_x, q_y) = \sum_{\gamma=-p}^p c_\gamma u_{kx,ky}^{i+\gamma+q_x, j+\gamma+q_y}$. We then define the matrix A to be the $(p+1)^2 \times (2p+1)(p+1)^2$ matrix given by

$$A = \frac{1}{2} \begin{bmatrix} c_{-p} \mathbb{I} & 0 & \dots & c_p \mathbb{I} & 0 \\ 0 & c_{-p} \mathbb{I} & 0 & 0 & c_p \mathbb{I} \\ & \ddots & \dots & \ddots & \\ 0 & & c_{-p} \mathbb{I} & 0 & c_p \mathbb{I} \end{bmatrix}$$

where the identity matrices are $(p+1)^2$. This is the actual matrix used in the summand. This matrix has the effect that

$$A \tilde{u}_{q_x, q_y}^{i, j} = \vec{a}^{i, j}(q_x, q_y)$$

where

$$\vec{a}^{i, j}(q_x, q_y) = [a_{r=0}^{i, j} \dots a_{r=p}^{i, j}]^T(q_x, q_y)$$

with

$$a_r^{i, j}(q_x, q_y) = [a_{0,r}^{i, j}(q_x, q_y) \dots a_{p,r}^{i, j}(q_x, q_y)]^T.$$

Hence, the seven coefficient matrices $K_{q_x, q_y}^{i, j}$ are defined by the composition

$$K_{q_x, q_y}^{i, j} = A \mathcal{C}^{q_x, q_y} \mathcal{S}^{i, j}$$

and have the effect

$$K_{q_x, q_y}^{i, j} u = \vec{a}^{i, j}(q_x, q_y).$$

197 Rather than concatenate these matrices at this point in the procedure, we will wait until after applying the
 198 projection to minimize the number of transformations performed. Note that each choice of (q_x, q_y) computes
 199 a different set of coefficients pertaining to a different set of basis functions.

200 **4.1.3. Projection Matrices.** Now to perform the projections. Because of the different filtered
 201 approximation forms in each quadrant, we must perform each projection slightly differently. Quadrants
 202 II and IV are similar as are I and III. Here we detail a procedure for QII.

QII. In QII we define the projection of this approximation by $u_h^f|_{K^{2i-1, 2j+1}}(x, y)$ where the new modal
 coefficients are computed by

$$(4.1) \quad \langle u_h^f, \phi_{kx} \phi_{ky} \rangle_{QII} = \langle u_h^f, \phi_{kx} \phi_{ky} \rangle_{QII}$$

$$(4.2) \quad = u_{kx,ky}^{2i-1, 2j+1}, \quad kx, ky = 0, \dots, p, \quad i, j = 1, \dots, N.$$

To account for the change in domain scaling define $\xi_x(\zeta_x) = \frac{\zeta_x - 1}{2}$ and $\xi_y(\zeta_y) = \frac{\zeta_y + 1}{2}$. We have

$$\begin{aligned} u_{kx,ky}^{2i-1, 2j+1} &= \sum_{m=0}^p \sum_{r=0}^p \int_{-1}^1 \int_{-1}^1 \left\{ a_{m,r}^{i,j}(-1, 0) \chi_{2T,L}^{m,r}(\xi_x, \xi_y) \right. \\ &\quad + a_{m,r}^{i,j}(0, 0) \chi_{2T,M}^{m,r}(\xi_x, \xi_y) \\ &\quad \left. + a_{m,r}^{i,j}(0, 1) \chi_{2T,R}^{m,r}(\xi_x, \xi_y) \right\} \phi_{kx}(\zeta_x) \phi_{ky}(\zeta_y) d\zeta_y d\zeta_x. \end{aligned}$$

203 This expression will be broken up into three separate integrals, one for each of the different $\chi_{(\cdot)}$ functions
204 where $(\cdot) \in \{L, M, R\}$. For each $\chi_{(\cdot)}$, define

$$P_{(\cdot)}(kx, ky, m, r) = \int_{-1}^1 \int_{-1}^1 \chi_{(2T, \cdot)}^{m, r}(\xi_x, \xi_y) \phi_{kx}(\zeta_x) \phi_{ky}(\zeta_y) d\zeta_y d\zeta_x.$$

Define the projection matrix $P_{(\cdot)}^{2T}$ by

$$P_{(\cdot)}^{2T} = \begin{bmatrix} \vec{P}(0, 0) \\ \vdots \\ \vec{P}(p, 0) \\ \vdots \\ \vec{P}(0, p) \\ \vdots \\ \vec{P}(p, p) \end{bmatrix},$$

where

$$\vec{P}(kx, ky) = [P(kx, ky, 0, 0) \dots P(kx, ky, p, 0) \dots \dots P(kx, ky, 0, p) \dots P(kx, ky, p, p)].$$

Hence, we have

$$u_{2i-1, 2j+1}^f = P_L^{2T} \vec{a}^{i,j}(-1, 0) + P_M^{2T} \vec{a}^{i,j}(0, 0) + P_R^{2T} \vec{a}^{i,j}(0, 1).$$

Noting the necessary choice of $K_{q_x, q_y}^{i,j}$ to obtain each of the coefficient vectors, we have

$$u_{2i-1, 2j+1}^f = (P_L^{2T} K_{-1, 0}^{i,j} + P_M^{2T} K_{0, 0}^{i,j} + P_R^{2T} K_{0, 1}^{i,j}) \vec{u}.$$

Denoting this composition by $T_{i,j}^{2T}$ we can concatenate these matrices together to obtain the global transition matrix T^{2T} defined by

$$T^{2T} = [T_{1,1}^{2T} \ \dots \ T_{N,1}^{2T} \ | \ \dots | \ T_{1,N}^{2T} \ \dots \ T_{N,N}^{2T}]^T,$$

such that

$$u_{2T}^f = T^{2T} \vec{u}.$$

205 **QIV.** The projection matrices for quadrant IV are the same except that the quadrant IV basis function
206 are used and the change of variables are instead $\xi_x(\zeta_x) = \frac{\zeta_x+1}{2}$ and $\xi_y(\zeta_y) = \frac{\zeta_y-1}{2}$.

QIII. The cases of quadrants I and III are similar in that a change of variables must be applied to split the integrals over the quadrant into a pair of integral over diagonals of that quadrant. Beginning with the integral over the whole quadrant, we have

$$\begin{aligned} \bar{u}_{kx, ky}^{2i-1, 2j-1} &= \langle u_h^*, \phi_{kx}^i \phi_{ky}^j \rangle_{QIII} \\ &= \int_{-1}^1 \int_{-1}^1 u_h^*|_{QIII}(\xi_x(\zeta_x), \xi_y(\zeta_y)) \phi_{kx}^i(\zeta_x) \phi_{ky}^j(\zeta_y) d\zeta_y d\zeta_x, \end{aligned}$$

where $\xi_x = \frac{\zeta_x-1}{2}$ and $\xi_y = \frac{\zeta_y-1}{2}$. Breaking this up into in an integral over $3T$ and $3B$ we have

$$\begin{aligned} \bar{u}_{kx, ky}^{2i-1, 2j-1} &= \int_{-1}^1 \int_{\zeta_x}^1 u_{3T}^*(\xi_x, \xi_y) \phi_{kx}^i(\zeta_x) \phi_{ky}^j(\zeta_y) d\zeta_y d\zeta_x \\ &+ \int_{-1}^1 \int_{-1}^{\zeta_x} u_{3B}^*(\xi_x, \xi_y) \phi_{kx}^i(\zeta_x) \phi_{ky}^j(\zeta_y) d\zeta_y d\zeta_x \end{aligned}$$

Now to use Gauss-Legendre quadrature we must scale the bounds of the inner integral to $[-1, 1]$. To do so introduce the change of variables $\zeta_y = \frac{1-\zeta_x}{2}\alpha_T + \frac{1+\zeta_x}{2}$ for the first integral and $\zeta_y = \frac{\zeta_x-1}{2}\alpha_B + \frac{1+\zeta_x}{2}$ for the second. This allows us to rewrite the expression as

$$\begin{aligned}\bar{u}_{kx,ky}^{2i-1,2j-1} &= \int_{-1}^1 \int_{-1}^1 u_{3T}^*(\xi_x, \xi_y(\zeta_y(\alpha_T))) \phi_{kx}^i(\zeta_x) \phi_{ky}^j \left(\frac{1}{2} [\alpha_T(1-\zeta_x) + 1 + \zeta_x] \right) \frac{1-\zeta_x}{2} d\alpha_T d\zeta_x \\ &\quad + \int_{-1}^1 \int_{-1}^1 u_{3B}^*(\xi_x, \xi_y(\zeta_y(\alpha_B))) \phi_{kx}^i(\zeta_x) \phi_{ky}^j \left(\frac{1}{2} [\alpha_B(\zeta_x - 1) + 1 + \zeta_x] \right) \frac{\zeta_x - 1}{2} d\alpha_B d\zeta_x. \\ &= \mathcal{J}^T + \mathcal{J}^B.\end{aligned}$$

We now need to split the \mathcal{J} terms into a sum of integrals over the basis functions and then multiply by the appropriate modal coefficients. Defining

$$P_{(\cdot)}^{3T}(kx, ky, m, r) = \int_{-1}^1 \int_{-1}^1 \chi_{3T,(\cdot)}^{m,r}(\xi_x, \xi_y(\alpha_T)) \phi_{kx}(\zeta_x) \phi_{ky}(\zeta_y(\alpha_T)) d\zeta_x d\alpha_T,$$

where $(\cdot) \in \{L, M, R\}$, we construct the projection matrices $P_L^{3T}, P_M^{3T}, P_R^{3T}$ in the same manner as in quadrant II. Now for the second set of integrals define

$$P_{(\cdot)}^{3B}(kx, ky, m, r) = \int_{-1}^1 \int_{-1}^1 \chi_{3B,(\cdot)}^{kx,ky}(\xi_x, \xi_y(\alpha_B)) \phi_{kx}(\zeta_x) \phi_{ky}(\zeta_y(\alpha_B)) d\zeta_x d\alpha_B,$$

and analogously construct the projection matrices $P_L^{3B}, P_M^{3B}, P_R^{3B}$. We then have

$$\begin{aligned}u_{2i-1,2j-1}^f &= P_L^{3T} \vec{a}^{i,j}(-1, -1) + P_M^{3T} \vec{a}^{i,j}(-1, 0) + P_R^{3T} \vec{a}^{i,j}(0, 0) \\ &\quad + P_L^{3B} \vec{a}^{i,j}(-1, -1) + P_M^{3B} \vec{a}^{i,j}(0, -1) + P_R^{3B} \vec{a}^{i,j}(0, 0).\end{aligned}$$

Now $\vec{a}^{i,j}(q_x, q_y) = K_{q_x, q_y}^{i,j} \vec{u}$, thus

$$u_{2i-1,2j-1}^f = \left[(P_L^{3T} + P_L^{3B}) K_{-1,-1}^{i,j} + (P_R^{3T} + P_R^{3B}) K_{0,0}^{i,j} + P_M^{3T} K_{-1,0}^{i,j} + P_M^{3B} K_{0,-1}^{i,j} \right] \vec{u}.$$

Denoting this composition by $T_{i,j}^3$ we can concatenate these matrices together to obtain the global transition matrix T^3 defined by

$$T^3 = [T_{1,1}^3 \quad \dots \quad T_{N,1}^3 \quad | \dots | \quad T_{1,N}^3 \quad \dots \quad T_{N,N}^3]^T,$$

such that

$$u_3^f = T^3 u.$$

207 **QI.** The case of quadrant one is that same as quadrant three except now $\xi_x = \frac{\zeta_x+1}{2}$, $\xi_y = \frac{\zeta_y+1}{2}$, and the
208 χ functions used are those defined on quadrant one.

209 **Coding Comment:** Note that forming global transition matrices is a memory intensive task, and
210 so we reduce the memory required at a single time by instead constructing $T_{i,j}^Q$ inside a nested for loop,
211 computing the new modal values while iterating over the elements. This approach requires less memory
212 than using concatenation to form the global transition matrices.

213 **4.2. Algorithm.** In the implementation, at some stage the transition matrices must be applied on an
214 element-by-element case. The reason being that constructing a global transition matrix for each quadrant or
215 octant results in a large $N^d(p+1)^d \times N^d(p+1)^d$ matrix which occupies considerable quantities of memory.
216 Though the filtering matrices have great sparsity which reduces their memory cost for storage, the projection
217 matrices are dense and this creates a memory bottleneck for a global realization. This leads to an alternative
218 pursued by the authors, that is to apply the projection procedure inside a loop over the mesh elements. We
219 provide a description of the this implementation in Algorithm 4.1

Algorithm 4.1 Calculate u^f from u using L-SIAC kernel

```

1: Input: Number of elements in one direction  $N$ , and polynomial degree  $p$ .
2: Output: Fine mesh modal coefficients  $u^f$ 
3:
4: % Compute modal projection on coarse mesh
5:  $u = \text{Initialize}(N, p, \Omega, u_0)$ 
6:
7: % Compute projection matrices by region
8:  $[P1TL, P1TM, P1TR] = \text{ProjMatrixL}(N, p, Q1T)$ 
9:  $[P1BL, P1BM, P1BR] = \text{ProjMatrixL}(N, p, Q1B)$ 
10:  $[P2TL, P2TM, P2TR] = \text{ProjMatrixL}(N, p, Q2T)$ 
11:  $[P3TL, P3TM, P3TR] = \text{ProjMatrixL}(N, p, Q3T)$ 
12:  $[P3BL, P3BM, P3BR] = \text{ProjMatrixL}(N, p, Q3B)$ 
13:  $[P4BL, P4BM, P4BR] = \text{ProjMatrixL}(N, p, Q4B)$ 
14:
15: % Loop through mesh elements
16: for  $i \leftarrow 1, N$  do
17:   for  $j \leftarrow 1, n$  do
18:
19:   % Construct filtering/sifting matrices
20:    $K11 = \text{FiltMatrixL}(p, 1, 1, i, j)$ 
21:    $K01 = \text{FiltMatrixL}(p, 0, 1, i, j)$ 
22:    $K10 = \text{FiltMatrixL}(p, 1, 0, i, j)$ 
23:    $K00 = \text{FiltMatrixL}(p, 0, 0, i, j)$ 
24:    $Kn10 = \text{FiltMatrixL}(p, -1, 0, i, j)$ 
25:    $K0n1 = \text{FiltMatrixL}(p, 0, -1, i, j)$ 
26:    $Kn1n1 = \text{FiltMatrixL}(p, -1, -1, i, j)$ 
27:
28:   % Compute local fine mesh coefficients
29:    $u_{\text{tensor}}^f(:, 2i, 2j) =$ 
30:      $((P1TL + P1BL) * K00 +$ 
31:      $(P1TR + P1BR) * K11 +$ 
32:      $(P1TM * K01 + P1BM * K10) * u$ 
33:    $u_{\text{tensor}}^f(:, 2i - 1, 2j) =$ 
34:      $(P2L * Kn10 + P2M * K00 + P2R * K01) * u$ 
35:    $u_{\text{tensor}}^f(:, 2i - 1, 2j - 1) =$ 
36:      $((P3TL + P3BL) * Kn1n1 +$ 
37:      $(P3TR + P3BR) * K00 +$ 
38:      $P3TM * Kn10 + P3BM * K0n1) * u$ 
39:    $u_{\text{tensor}}^f(:, 2i, 2j - 1) =$ 
40:      $(P4L * K0n1 + P4M * K00 + P4R * K10) * u$ 
41:
42: end for
43: end for
44:
45: % Reshape fine modal array into original array form
46:  $u^f = \text{ReshapeArray}(p, N, u_{\text{tensor}}^f)$ 

```

²²⁰ **5. Numerical Results.** The goal of LSIAC-MRA is to produce a fine-mesh modal approximation from
²²¹ coarse-mesh data that has lower error than repeated L^2 -projection alone. The measures used for comparison

222 are the L^2 – and L^∞ – errors defined respectively by

$$(5.1) \quad \begin{aligned} \|u_{exact} - u_{approx}\|_0 &= \sqrt{\frac{1}{|\Omega|} \int_{\Omega} |u_{exact} - u_{approx}|^2 d\Omega}, & \|u_{exact} - u_{approx}\|_\infty &= \sup_{x \in \Omega} |u_{exact} - u_{approx}|. \end{aligned}$$

223 For our simulations, the L^2 error is evaluated through Gauss-Legendre quadrature at 6^d nodes per element.
224 Similarly, the L^∞ is taken to be the maximum error over these nodes. In all the simulations considered below,
225 periodic boundary conditions are assumed to allow the application of the filter in regions where the kernel
226 support would surpass the domain boundaries. To display the ability of LSIAC-MRA filtering-projection
227 procedure, we perform the following two- and three-dimensional tests.

228 **5.1. 2D Test Problems.** Consider the following functions on the domain $\Omega = \{(x, y) \in [0, 1]^2\} :$

- 229 1. $u_0(x, y) = \sin(2\pi x) \sin(2\pi y),$
- 230 2. $u_0(x, y) = \sin(2\pi x) + \sin(2\pi y),$
- 231 3. $u_0(x, y) = \sin(2\pi(x + y)).$

232 These test functions aid us in evaluating the effectiveness of the LSIAC-MRA procedure. The first function
233 is a tensor product of the coordinate directions, while the second is a sum. The last function can be viewed
234 as a combination of a product and summation of the coordinate directions. Note that we only present the
235 second two functions as the first function performs similarly.

236 Beginning with a projection of these functions onto a piecewise orthonormal Legendre basis on a 35×35
237 uniform quadrilateral mesh, the approximation is then enhanced by the LSIAC-MRA. This procedure is
238 applied two times, resulting in a final approximation on a 140×140 mesh. The L^2 – and L^∞ – errors of those
239 approximations with and without the filtering enhancement are given in Tables 5.1 and 5.2.

240 The first two columns of the tables detail the projections errors of the L^2 approximation subject to scale
241 transition by projection without filtering. This represents the standard which our filtered approximations
242 must outperform to justify the computational expense. The third and fourth columns detail the errors of
243 an approximation when LSIAC-MRA is applied only once and then L^2 – projection is used. The final two
244 columns detail the errors of the LSIAC-MRA procedure applied at each refinement. As a result, the first
245 rows will agree for all approximations as each begins as a L^2 – projection onto the coarse mesh. Similarly,
246 the Enhanced Once and Enhanced Each Refinement columns will agree on the second mesh $N = 30$ simply
247 because only one filtering procedure has been applied at that point. We observe that application of the
248 filtering procedure at each stage continues to provide error reductions with each refinement and outperforms
249 only applying the filtering procedure once.

250 As depicted in the log-log plots in Figures 5.3, and 5.4, the L-SIAC filter does indeed provide an error
251 reduction. These techniques are not guaranteed to improve the order of the method, however they provide
252 a reduced error constant.

253 The choice of filter alters not only the magnitude globally of errors, but also their pointwise distribution.
254 The contour plots in Figures 5.1 and 5.2 display that repeated enhancement will lead to a homogenization
255 of the pointwise errors, though a single application of LSIAC-MRA. This demonstrates how LSIAC-MRA
256 will alter not only the magnitude of the errors, but also the distribution of errors throughout the domain.

257 **5.2. 3D Test Problems.** We now investigate the application of these techniques for the

258 three-dimensional counterparts of the functions above. Consider the following functions on the domain
259 $\Omega = \{(x, y) \in [0, 1]^3\} :$

- 260 1. $u_0(x, y, z) = \sin(2\pi x) \sin(2\pi y) \sin(2\pi z),$
- 261 2. $u_0(x, y, z) = \sin(2\pi x) + \sin(2\pi y) + \sin(2\pi z),$
- 262 3. $u_0(x, y, z) = \sin(2\pi(x + y + z)).$

263 Again we present the results of the latter two function to illustrate the performance of the LSIAC-MRA
264 procedure in 3D.

265 Beginning with a projection of these functions onto a piecewise orthonormal Legendre basis on a $15 \times$
266 15×15 uniform hexahedral mesh, the approximation is then enhanced using the LSIAC-MRA procedure.
267 This procedure is applied two times, resulting in a final approximation on a $60 \times 60 \times 60$ mesh. The L^2 – and
268 L^∞ – errors of those approximations with and without the filtering enhancement are given in Tables 5.3 and
269 5.4. Notice that we have included the results for a piecewise constant approximation, $p = 0$. The theory of
270 (L)SIAC does not generally extend to piecewise constants. However, it is evident from the results in these

271 tables that the LSIAC-MRA procedure is effective for piecewise constant approximations. For piecewise
 272 linear approximations, $p = 1$, we can see that it is less effective, but still provides an error reduction. We
 273 speculate that for higher degree polynomial approximations, it is necessary to start with a higher resolution
 274 in order for the LSIAC-MRA procedure to be more effective. The the log-log plots for the results of the 3D
 275 LSIAC-MRA procedure are given in Figures 5.5 and 5.6.

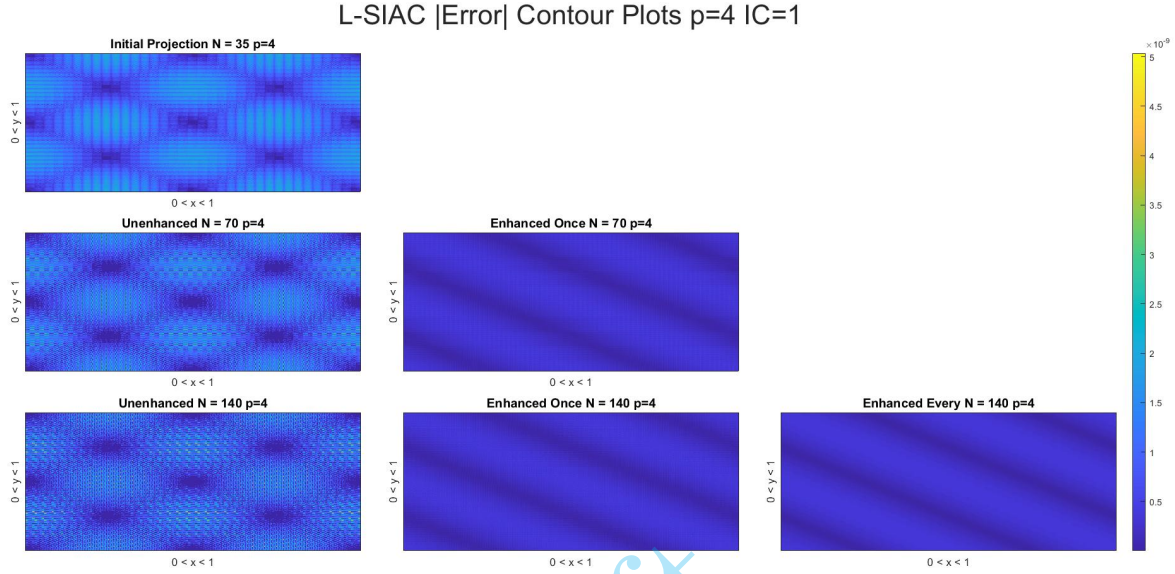


Fig. 5.1: Contour plots depicting pointwise $|\text{Error}|$ for initial condition $u(x, y) = \sin(2\pi x) \sin(2\pi y)$ on a series of three meshes using the **2D L-SIAC** filter $p = 4$. Notice that the filtering procedure alters the pointwise distribution of the error, and maintains this new distribution with further mesh refinement.

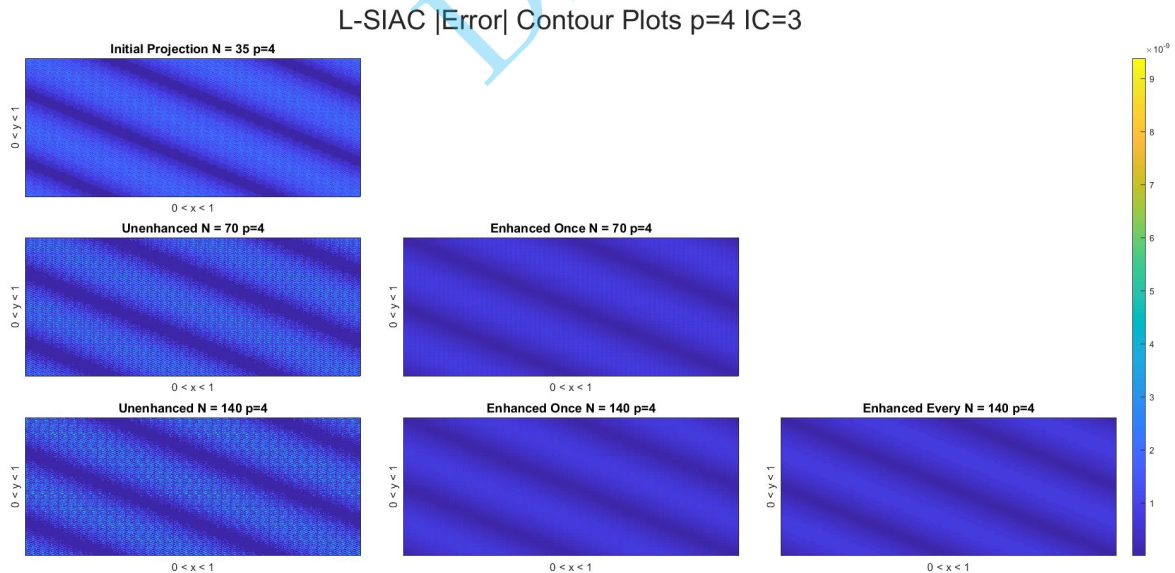


Fig. 5.2: Contour plots depicting pointwise $|\text{Error}|$ for initial condition $u(x, y) = \sin(2\pi(x + y))$ on a series of three meshes using the **2D L-SIAC** filter $p = 4$. Notice that the filtering procedure appears to regularize errors along a direction perpendicular to the kernel orientation.

Table 5.1: Table of L^2 and L^∞ errors for initial condition $u(x, y) = \sin(2\pi x) + \sin(2\pi y)$ on a series of four meshes using the **2D L-SIAC** filter. Notice that performing the enhancement procedure once causes a one-time reduction in errors. Applying the enhancement procedure with each mesh refinement continues to reduce the errors.

N	Projection Error		Enhanced Once		Enhanced Each Refinement	
	L^2 -Error	L^∞ -Error	L^2 -Error	L^∞ -Error	L^2 -Error	L^∞ -Error
\mathbb{P}^1						
35	1.45e-04	2.41e-03	1.45e-04	2.41e-03	1.45e-04	2.41e-03
70	2.04e-04	2.56e-03	5.16e-05	5.81e-04	5.16e-05	5.81e-04
140	1.44e-04	2.70e-03	3.64e-05	6.44e-04	1.02e-05	1.70e-04
\mathbb{P}^2						
35	3.76e-06	6.05e-05	3.76e-06	6.05e-05	3.76e-06	6.05e-05
70	5.32e-06	7.76e-05	6.69e-07	7.61e-06	6.69e-07	7.61e-06
140	4.06e-06	8.67e-05	4.73e-07	9.74e-06	6.59e-08	1.09e-06
\mathbb{P}^3						
35	2.48e-08	2.92e-07	2.48e-08	2.92e-07	2.48e-08	2.92e-07
70	3.50e-08	4.55e-07	2.34e-09	2.12e-08	2.34e-09	2.12e-08
140	2.48e-08	5.55e-07	1.69e-09	3.12e-08	2.92e-10	3.69e-09
\mathbb{P}^4						
35	3.84e-10	4.12e-09	3.84e-10	4.12e-09	3.84e-10	4.12e-09
70	5.43e-10	6.78e-09	1.74e-11	1.34e-10	1.74e-11	1.34e-10
140	4.18e-10	9.37e-09	1.23e-11	2.18e-10	6.32e-13	9.11e-12

Table 5.2: Table of L^2 and L^∞ errors for initial condition $u(x, y) = \sin(2\pi(x + y))$ on a series of four meshes using the **2D L-SIAC** filter. Notice that performing the enhancement procedure once causes a one-time reduction in errors. Applying the enhancement procedure with each mesh refinement continues to reduce the errors.

N	Projection Error		Enhanced Once		Enhanced Each Refinement	
	L^2 -Error	L^∞ -Error	L^2 -Error	L^∞ -Error	L^2 -Error	L^∞ -Error
\mathbb{P}^1						
35	2.03e-04	4.32e-03	2.03e-04	4.32e-03	2.03e-04	4.32e-03
70	2.87e-04	4.84e-03	7.44e-05	1.02e-03	7.44e-05	1.02e-03
140	2.15e-04	5.10e-03	5.25e-05	1.15e-03	1.75e-05	2.47e-04
\mathbb{P}^2						
35	3.08e-06	6.05e-05	3.08e-06	6.05e-05	3.08e-06	6.05e-05
70	4.35e-06	7.77e-05	6.19e-07	8.53e-06	6.19e-07	8.53e-06
140	3.26e-06	8.68e-05	4.65e-07	1.05e-05	2.46e-07	3.14e-06
\mathbb{P}^3						
35	3.48e-08	5.29e-07	3.48e-08	5.29e-07	3.48e-08	5.29e-07
70	4.92e-08	8.49e-07	6.38e-09	6.47e-08	6.38e-09	6.47e-08
140	3.88e-08	1.03e-06	4.54e-09	8.46e-08	3.85e-09	3.51e-08
\mathbb{P}^4						
35	3.14e-10	4.12e-09	3.14e-10	4.12e-09	3.14e-10	4.12e-09
70	4.44e-10	6.79e-09	1.28e-10	8.87e-10	1.28e-10	8.87e-10
140	3.36e-10	9.39e-09	9.17e-11	9.05e-10	9.08e-11	7.76e-10

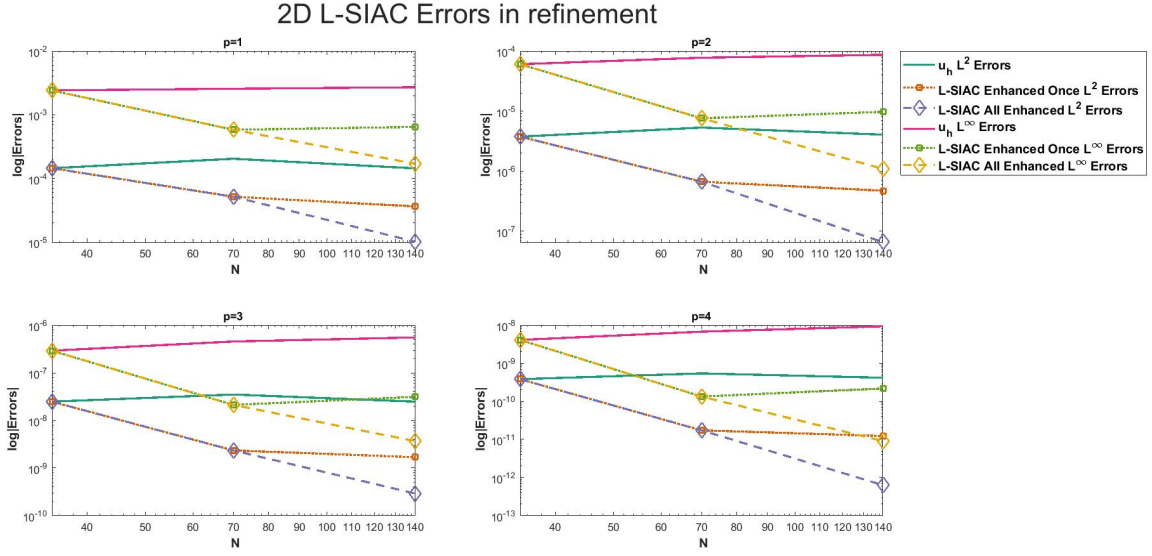


Fig. 5.3: Log-log plots of N vs. $|\text{Error}|$ for the function $u(x, y) = \sin(2\pi x) + \sin(2\pi y)$ on a series of three meshes using the **2D L-SIAC** filter.

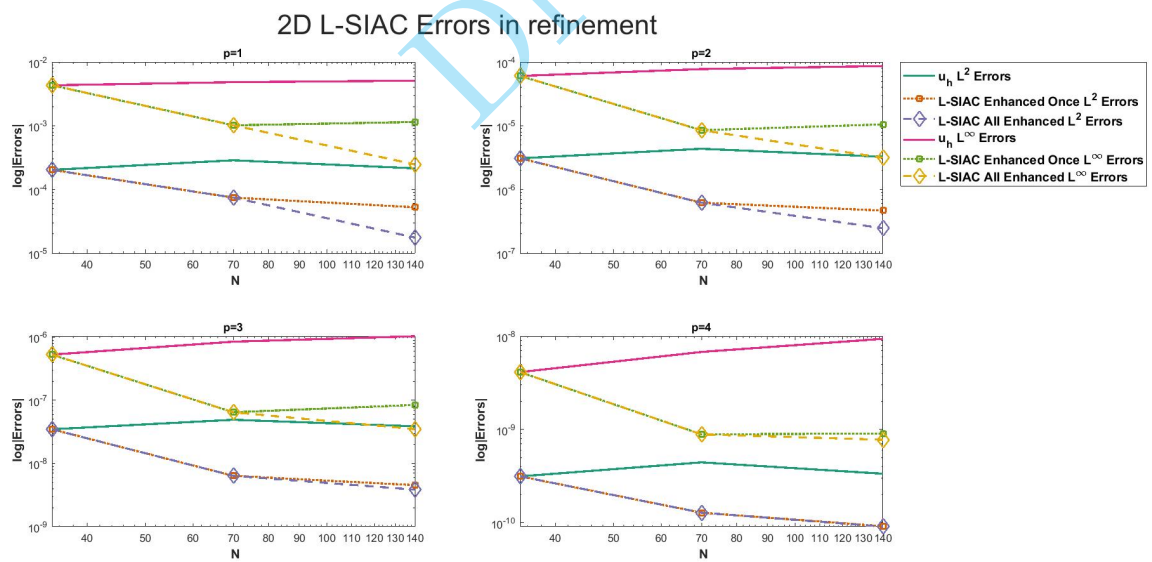


Fig. 5.4: Log-log plots of N vs. $|\text{Error}|$ for the function $u(x, y) = \sin(2\pi(x + y))$ on a series of three meshes using the **2D L-SIAC** filter. Notice that mesh refinement with filtering out performs mesh refinement alone.

Table 5.3: Table of L^2 and L^∞ errors for initial condition $u(x, y, z) = \sin(2\pi x) + \sin(2\pi y) + \sin(2\pi z)$ on a series of three meshes using the **3D L-SIAC** filter.

N	Projection Error		Enhanced Once		Enhanced Each Refinement	
	L^2 -Error	L^∞ -Error	L^2 -Error	L^∞ -Error	L^2 -Error	L^∞ -Error
\mathbb{P}^0						
15	4.36e-02	5.82e-01	4.36e-02	5.82e-01	4.36e-02	5.82e-01
30	8.78e-02	6.03e-01	4.46e-02	2.96e-01	4.46e-02	2.96e-01
60	7.28e-02	6.13e-01	3.15e-02	3.06e-01	1.72e-02	1.55e-01
\mathbb{P}^1						
15	1.72e-03	2.62e-02	1.72e-03	2.62e-02	1.72e-03	2.62e-02
30	3.42e-03	2.84e-02	9.00e-04	6.18e-03	9.00e-04	6.18e-03
60	2.43e-03	3.00e-02	6.32e-04	6.84e-03	2.39e-04	3.29e-03

Table 5.4: Table of L^2 and L^∞ errors for initial condition $u(x, y, z) = \sin(2\pi(x + y + z))$ on a series of three meshes using the **3D L-SIAC** filter.

N	Projection Error		Enhanced Once		Enhanced Each Refinement	
	L^2 -Error	L^∞ -Error	L^2 -Error	L^∞ -Error	L^2 -Error	L^∞ -Error
\mathbb{P}^0						
15	3.81e-02	5.76e-01	3.81e-02	5.76e-01	3.81e-02	5.76e-01
30	7.61e-02	5.95e-01	4.92e-02	3.09e-01	4.92e-02	3.09e-01
60	6.01e-02	6.05e-01	3.53e-02	3.19e-01	3.16e-02	1.91e-01
\mathbb{P}^1						
15	2.06e-03	3.54e-02	2.06e-03	3.54e-02	2.06e-03	3.54e-02
30	4.13e-03	3.97e-02	4.13e-03	1.58e-02	4.13e-03	1.58e-02
60	3.03e-03	4.20e-02	2.88e-03	1.65e-02	2.93e-03	1.32e-02

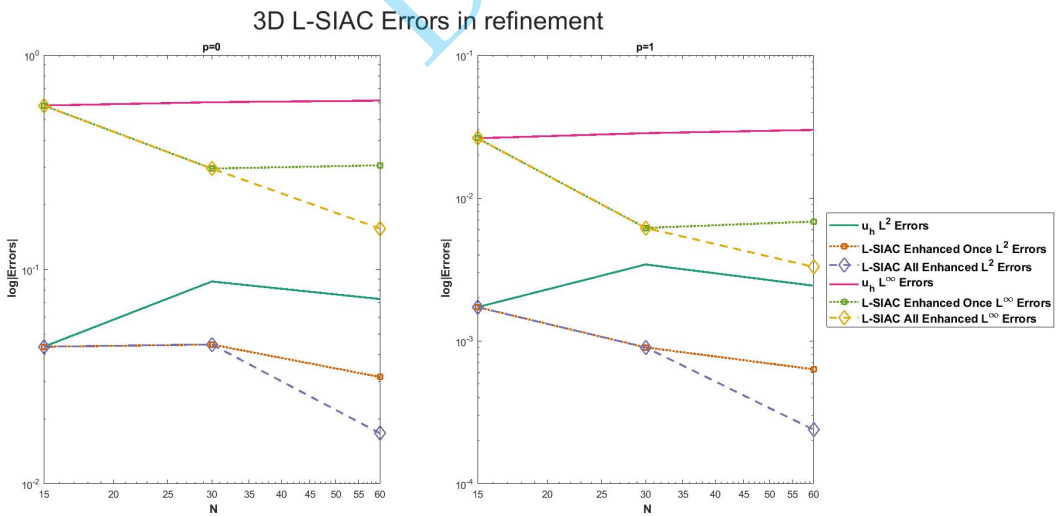


Fig. 5.5: Log-log plots of N vs. $|\text{Error}|$ for the function $u(x, y, z) = \sin(2\pi x) + \sin(2\pi y) + \sin(2\pi z)$ on a series of three meshes using the **3D L-SIAC** filter. Notice that mesh refinement with filtering out performs mesh refinement alone.



Fig. 5.6: Log-log plots of N vs. $|\text{Error}|$ for the function $u(x, y, z) = \sin(2\pi(x + y + z))$ on a series of three meshes using the **3D L-SIAC** filter. Notice that mesh refinement with filtering out performs mesh refinement alone. The initial mesh is likely too coarse to allow for further approximation improvement.

276 **6. Conclusions and Future Work.** In this article, we have introduced an improved multi-resolution
 277 analysis scheme for multi-dimensional applications, LSIAC-MRA. This scheme utilizes the Line Smoothness-
 278 Increasing Accuracy-Conserving filter which post-processes multi-dimensional data using a one-dimensional
 279 support to approximate the difference coefficients that allows for reducing the error with mesh refinement.
 280 We provide the underlying operational framework, algorithm, and demonstrate that it is effective for two-
 281 and three-dimensional applications. Furthermore, contrary to the theory of SIAC filters, it is effective for
 282 multi-dimensional piecewise constant data. In the future, we plan on investigating the requirements for the
 283 points per wavelength of the initial data as well as allowed non-uniformities in the data in order to leverage
 284 LSIAC-MRA for turbulence modeling data or improved identification of undersampled signals.

285 **7. Acknowledgements.** This work is partially supported by AFOSR under grant number FA9550-
 286 20-1-0166. We would like to thank Dr. Ayaboe Edoh and Dr. Xulia Docampo-Sánchez for their valuable
 287 comments in the presentation of this paper.

288 **Statement of Contribution.** The ideas in this article were conceived by Jennifer Ryan, who is also
 289 responsible for the presentation of information, writing the introduction and conclusion sections, and final
 290 edits. Matt Picklo performed the numerical experiments and wrote the majority of the article.

291

REFERENCES

- 292 [1] B.K. Alpert. A Class of Bases in L^2 for the Sparse Representation of Integral Operators. *SIAM Journal on Mathematical*
 293 *Analysis*, 24:246–262, 1993.
- 294 [2] B.K. Alpert, G. Beylkin, D. Gines, and L. Vozovoi. Adaptive Solution of Partial Differential Equations in Multiwavelet
 295 Bases. *Journal of Computational Physics*, 182:149–190, 2002.
- 296 [3] Albert Boggess and Francis J. Narcowich. *A First Course in Wavelets with Fourier Analysis*. Prentice Hall, Upper Saddle,
 297 New Jersey, 2001.
- 298 [4] B. Cockburn, M. Luskin, C.-W. Shu, and E. Suli. Enhanced accuracy by post-processing for finite element methods for
 299 hyperbolic equations. *Mathematics of Computation*, 72:577–606, 2003.
- 300 [5] Albert Cohen. *Numerical Analysis of Wavelet Methods*. Elsevier, Amsterdam, 2003.
- 301 [6] A. Dedner, J. Giesselmann, T. Pryer, and J.K. Ryan. Residual estimates for post-processors in elliptic problems. *Journal*
 302 *of Scientific Computing*, 88, 2021.
- 303 [7] J. Docampo, G.B. Jacobs, X.Li, and J.K. Ryan. Enhancing accuracy with a convolution filter: What works and why!
 304 *Computers and Fluids*, 213, 2020.
- 305 [8] Julia Docampo-Sánchez, Jennifer K. Ryan, Mahsa Mirzargar, and Robert M. Kirby. Multi-dimensional filtering: Reducing
 306 the dimension through rotation. *SIAM Journal on Scientific Computing*, 39:A2179–A2200, 2017.
- 307 [9] N. Hovhannyan, S. Müller, and R. Schäfer. Adaptive Multiresolution Discontinuous Galerkin Schemes for Conservation
 308 Laws. Report 311, Institut für Geometrie und Praktische Mathematik, Aachen, sep 2010. <http://www.igpm.rwth-aachen.de/en/reports2010>.
- 310 [10] Liangyue Ji, Paulien van Slingerland, Jennifer K. Ryan, and Kees Vuik. Superconvergent Error Estimates for a Position-
 311 Dependent Smoothness-Increasing Accuracy-Conserving filter for DG Solutions. *Mathematics of Computation*,
 312 83:2239–2262, 2014.
- 313 [11] Liangyue Ji, Yan Xu, and Jennifer K. Ryan. Accuracy enhancement for the linear convection-diffusion equation in multiple
 314 dimensions. *Mathematics of Computation*, 81:1929–1950, 2012.
- 315 [12] Liangyue Ji, Yan Xu, and Jennifer K. Ryan. Negative-order norm estimates for nonlinear hyperbolic conservation laws.
 316 *Journal of Scientific Computing*, 54:269–310, 2013.
- 317 [13] Xiong Meng and Jennifer K. Ryan. Discontinuous Galerkin methods for nonlinear scalar hyperbolic conservation laws:
 318 divided difference estimates and accuracy enhancement. *Numerische Mathematik*, 136:27–73, 2017.
- 319 [14] Xiong Meng and Jennifer K. Ryan. Divided difference estimates and accuracy enhancement of discontinuous Galerkin
 320 methods for nonlinear symmetric systems of hyperbolic conservation laws. *IMA Journal of Numerical Analysis*,
 321 38:125–155, 2018.
- 322 [15] Evert Johannes Nyström. Über die praktische auflösung von integralgleichungen mit anwendungen auf randwertaufgaben.
 323 *Acta Mathematica*, 54:185–204, 1930.
- 324 [16] Jennifer K. Ryan. Capitalizing on superconvergence for more accurate multi-resolution discontinuous galerkin methods.
 325 *Communications in Applied Mathematics and Computation*, 2021.
- 326 [17] Jennifer K. Ryan and Bernardo Cockburn. Local derivative post-processing for the discontinuous Galerkin method. *Journal*
 327 *of Computational Physics*, 228:8642 –8664, 2009.
- 328 [18] Jennifer K. Ryan, Xiaozhou Li, Robert M. Kirby, and Kees Vuik. One-sided position-dependent Smoothness-Increasing
 329 Accuracy-Conserving (SIAC) filtering over uniform and non-uniform meshes. *Journal of Scientific Computing*, 64:773–
 330 817, 2015.
- 331 [19] Jennifer K. Ryan and Chi-Wang Shu. One-sided post-processing for the discontinuous Galerkin method. *Methods and*
 332 *Applications of Analysis*, 10:295 – 307, 2003.
- 333 [20] Jennifer K. Ryan, Chi-Wang Shu, and Harold Atkins. Extension of a post-processing technique for the discontinuous
 334 Galerkin method for hyperbolic equations with application to an aeroacoustic problem. *SIAM Journal on Scientific*
 335 *Computing*, 26:821–843, 2005.

336 [21] Paulien van Slingerland, Jennifer K. Ryan, and Kees Vuik. Position-Dependent Smoothness-Increasing Accuracy-
337 Conserving (SIAC) Filtering for Accuracy for Improving discontinuous Galerkin solutions. *SIAM Journal on Scientific
338 Computing*, 33:802–825, 2011.

Draft

³³⁹ **8. Supplementary Materials.** The following materials contain the χ functions and associated
³⁴⁰ coefficients appearing in the filtered approximation forms for the one-, two-, and three-dimensional cases.
³⁴¹ Denote by ζ the mapping of the filtering point to the reference element $[-1, 1]$, i.e. $\zeta_x = \frac{2}{h}(x - x_i)$,
³⁴² $\zeta_y = \frac{2}{h}(y - y_j)$, $\zeta_z = \frac{2}{h}(z - z_k)$.

³⁴³ **One-dimensional SIAC.** The one-dimensional filtered approximation is of the form

$$u_h^*(x) = \begin{cases} \sum_{m=0}^{p+1} d_m^j \chi_L^m(\zeta_x), & \zeta_x \in (-1, 0) \\ \sum_{m=0}^{p+1} \tilde{d}_m^j \chi_R^m(\zeta_x), & \zeta_x \in (0, 1) \end{cases},$$

³⁴⁴ with the χ functions and coefficients given in Table (8.1).

Table 8.1: Table of basis functions and associated coefficients resulting from the analytical evaluation of the convolution in $u_h^*(x)$.

\mathbf{k}	$d_{\mathbf{k}}^j$	$\tilde{d}_{\mathbf{k}}^j$
0	$\frac{\sqrt{2}}{2} \left[\sum_{\gamma=-p}^p c_{\gamma} u_0^{j+\gamma} \right]$	$\frac{\sqrt{2}}{2} \left[\sum_{\gamma=-p}^p c_{\gamma} u_0^{j+\gamma} \right]$
1	$\frac{\sqrt{2}}{4} \left[\sum_{\gamma=-p}^p c_{\gamma} (u_0^{j+\gamma} - u_0^{j+\gamma-1}) \right]$	$\frac{\sqrt{2}}{4} \left[\sum_{\gamma=-p}^p c_{\gamma} (u_0^{j+\gamma+1} - u_0^{j+\gamma}) \right]$
$\mathbf{k} > 1$	$\frac{1}{2} \left[\sum_{\gamma=-p}^p c_{\gamma} (u_k^{j+\gamma} - u_k^{j+\gamma-1}) \right]$	$\frac{1}{2} \left[\sum_{\gamma=-p}^p c_{\gamma} (u_k^{j+\gamma+1} - u_k^{j+\gamma}) \right]$
\mathbf{k}	$\chi_{\mathbf{L}}^{\mathbf{k}}(\zeta)$	$\chi_{\mathbf{R}}^{\mathbf{k}}(\zeta)$
0.	1	1
1.	ζ	ζ
$\mathbf{k} > 1.$	$\frac{\sqrt{k-1/2}}{2k-1} \left[P_k(1 + \zeta) - P_{k-2}(1 + \zeta) \right]$	$\frac{\sqrt{k-1/2}}{2k-1} \left[P_k(\zeta - 1) - P_{k-2}(\zeta - 1) \right]$

³⁴⁵ **Two-dimensional L-SIAC.** The basis for two-dimensional L-SIAC filtered approximation is given in
³⁴⁶ Table 8.2. This is a result of the kernel support overlapping different elements based on the region in which
³⁴⁷ the filtering point is located. There are seven associated coefficients of the form

$$a_{R,P,m,r} = a_{m,r}(q_x, q_y) = \sum_{\gamma=-p}^p c_{\gamma} u_{m,r}^{i+\gamma+q_x, j+\gamma+q_y},$$

³⁴⁸ where the arguments (q_x, q_y) are determined by the region S and position P of the filter point. A table of
³⁴⁹ these dependencies by region and position is provided in Table 8.3.

Table 8.2: 2D L-SIAC basis functions. For notational convenience suppose \mathbf{x} belongs to element (i, j) .

Region S	Basis Function	Definition
1T	$\chi_{1T,L}^{m,r}(\zeta_x, \zeta_y)$	$\frac{2-\zeta_y}{2} \int_{-1}^1 \phi_{kx} \left(\zeta_x - \frac{\zeta_y}{2} + \left(1 - \frac{\zeta_y}{2}\right) \eta \right) \phi_{ky} \left(\left(1 - \frac{\zeta_y}{2}\right) \eta + \frac{\zeta_y}{2} \right) d\eta$
	$\chi_{1T,M}^{m,r}(\zeta_x, \zeta_y)$	$\frac{\zeta_y - \zeta_x}{2} \int_{-1}^1 \phi_{kx} \left(\frac{\zeta_y - \zeta_x}{2} \eta + \frac{\zeta_x - \zeta_y}{2} + 1 \right) \phi_{ky} \left(\frac{\zeta_y - \zeta_x}{2} \eta + \frac{\zeta_y - \zeta_x}{2} - 1 \right) d\eta$
	$\chi_{1T,R}^{m,r}(\zeta_x, \zeta_y)$	$\frac{\zeta_x}{2} \int_{-1}^1 \phi_{kx} \left(\frac{\zeta_x}{2} \eta + \frac{\zeta_x}{2} - 1 \right) \phi_{ky} \left(\frac{\zeta_x}{2} \eta + \zeta_y - 1 - \frac{\zeta_x}{2} \right) d\eta$
1B	$\chi_{1B,L}^{m,r}(\zeta_x, \zeta_y)$	$\frac{2-\zeta_x}{2} \int_{-1}^1 \phi_{kx} \left(\left(1 - \frac{\zeta_x}{2}\right) \eta + \frac{\zeta_x}{2} \right) \phi_{ky} \left(\zeta_y - \frac{\zeta_x}{2} + \left(1 - \frac{\zeta_x}{2}\right) \eta \right) d\eta$
	$\chi_{1B,M}^{m,r}(\zeta_x, \zeta_y)$	$\frac{\zeta_x - \zeta_y}{2} \int_{-1}^1 \phi_{kx} \left(\frac{\zeta_x - \zeta_y}{2} \eta + \frac{\zeta_x - \zeta_y}{2} - 1 \right) \phi_{ky} \left(\frac{\zeta_x - \zeta_y}{2} \eta + \frac{\zeta_y - \zeta_x}{2} + 1 \right) d\eta$
	$\chi_{1B,R}^{m,r}(\zeta_x, \zeta_y)$	$\frac{\zeta_y}{2} \int_{-1}^1 \phi_{kx} \left(\frac{\zeta_y}{2} \eta + \zeta_x - \frac{\zeta_y}{2} - 1 \right) \phi_{ky} \left(\frac{\zeta_y}{2} \eta - 1 + \frac{\zeta_y}{2} \right) d\eta$
2T	$\chi_{2T,L}^{m,r}(\zeta_x, \zeta_y)$	$-\frac{\zeta_x}{2} \int_{-1}^1 \phi_{kx} \left(-\frac{\zeta_x}{2} \eta + \frac{\zeta_x}{2} + 1 \right) \phi_{ky} \left(-\frac{\zeta_x}{2} \eta + \zeta_y - 1 - \frac{\zeta_x}{2} \right) d\eta$
	$\chi_{2T,M}^{m,r}(\zeta_x, \zeta_y)$	$\frac{2+\zeta_x - \zeta_y}{2} \int_{-1}^1 \phi_{kx} \left(\frac{2+\zeta_x - \zeta_y}{2} \eta + \frac{\zeta_x - \zeta_y}{2} \right) \phi_{ky} \left(\frac{2+\zeta_x - \zeta_y}{2} \eta + \frac{\zeta_y - \zeta_x}{2} \right) d\eta$
	$\chi_{2T,R}^{m,r}(\zeta_x, \zeta_y)$	$\frac{\zeta_y}{2} \int_{-1}^1 \phi_{kx} \left(\frac{\zeta_y}{2} \eta + \zeta_x - \frac{\zeta_y}{2} + 1 \right) \phi_{ky} \left(\frac{\zeta_y}{2} \eta + \frac{\zeta_y}{2} - 1 \right) d\eta$
3T	$\chi_{3T,L}^{m,r}(\zeta_x, \zeta_y)$	$-\frac{\zeta_y}{2} \int_{-1}^1 \phi_{kx} \left(-\frac{\zeta_y}{2} \eta - \frac{\zeta_y}{2} + \zeta_x + 1 \right) \phi_{ky} \left(-\frac{\zeta_y}{2} \eta + 1 + \frac{\zeta_y}{2} \right) d\eta$
	$\chi_{3T,M}^{m,r}(\zeta_x, \zeta_y)$	$\frac{\zeta_y - \zeta_x}{2} \int_{-1}^1 \phi_{kx} \left(\frac{\zeta_y - \zeta_x}{2} \eta + \frac{\zeta_x - \zeta_y}{2} + 1 \right) \phi_{ky} \left(\frac{\zeta_y - \zeta_x}{2} \eta + \frac{\zeta_y - \zeta_x}{2} - 1 \right) d\eta$
	$\chi_{3T,R}^{m,r}(\zeta_x, \zeta_y)$	$\frac{2+\zeta_x}{2} \int_{-1}^1 \phi_{kx} \left(\left(\frac{2+\zeta_x}{2} \right) \eta + \frac{\zeta_x}{2} \right) \phi_{ky} \left(\left(\frac{2+\zeta_x}{2} \right) \eta - \frac{\zeta_x}{2} + \zeta_y \right) d\eta$
3B	$\chi_{3B,L}^{m,r}(\zeta_x, \zeta_y)$	$-\frac{\zeta_x}{2} \int_{-1}^1 \phi_{kx} \left(-\frac{\zeta_x}{2} \eta + \frac{\zeta_x}{2} + 1 \right) \phi_{ky} \left(-\frac{\zeta_x}{2} \eta + 1 + \zeta_y - \frac{\zeta_x}{2} \right) d\eta$
	$\chi_{3B,M}^{m,r}(\zeta_x, \zeta_y)$	$\frac{\zeta_x - \zeta_y}{2} \int_{-1}^1 \phi_{kx} \left(\frac{\zeta_x - \zeta_y}{2} \eta + \frac{\zeta_x - \zeta_y}{2} - 1 \right) \phi_{ky} \left(\frac{\zeta_x - \zeta_y}{2} \eta + \frac{\zeta_y - \zeta_x}{2} + 1 \right) d\eta$
	$\chi_{3B,R}^{m,r}(\zeta_x, \zeta_y)$	$\frac{2+\zeta_y}{2} \int_{-1}^1 \phi_{kx} \left(\left(\frac{2+\zeta_y}{2} \right) \eta + \zeta_x - \frac{\zeta_y}{2} \right) \phi_{ky} \left(\left(\frac{2+\zeta_y}{2} \right) \eta + \frac{\zeta_y}{2} \right) d\eta$
4B	$\chi_{4B,L}^{m,r}(\zeta_x, \zeta_y)$	$-\frac{\zeta_y}{2} \int_{-1}^1 \phi_{kx} \left(-\frac{\zeta_y}{2} \eta - \frac{\zeta_y}{2} + \zeta_x - 1 \right) \phi_{ky} \left(-\frac{\zeta_y}{2} \eta + 1 + \frac{\zeta_y}{2} \right) d\eta$
	$\chi_{4B,M}^{m,r}(\zeta_x, \zeta_y)$	$\frac{\zeta_y - \zeta_x + 2}{2} \int_{-1}^1 \phi_{kx} \left(\left(1 + \frac{\zeta_y - \zeta_x}{2} \right) \eta + \frac{\zeta_x - \zeta_y}{2} \right) \phi_{ky} \left(\left(1 + \frac{\zeta_y - \zeta_x}{2} \right) \eta + \frac{\zeta_y - \zeta_x}{2} \right) d\eta$
	$\chi_{4B,R}^{m,r}(\zeta_x, \zeta_y)$	$\frac{\zeta_x}{2} \int_{-1}^1 \phi_{kx} \left(\frac{\zeta_x}{2} \eta + \frac{\zeta_x}{2} - 1 \right) \phi_{ky} \left(\frac{\zeta_x}{2} \eta + 1 + \zeta_y - \frac{\zeta_x}{2} \right) d\eta$

Table 8.3: Table describing how the shifting of the arguments of the a coefficients vary by region.

Region (S) \ Arguments of $a_\alpha(q_x, q_y)$	$\mathbf{P} = \mathbf{L}$	$\mathbf{P} = \mathbf{M}$	$\mathbf{P} = \mathbf{R}$
1T	(0, 0)	(0, 1)	(1, 1)
1B	(0, 0)	(1, 0)	(1, 1)
2T	(-1, 0)	(0, 0)	(0, 1)
3T	(-1, -1)	(-1, 0)	(0, 0)
3B	(-1, -1)	(0, -1)	(0, 0)
4B	(0, -1)	(0, 0)	(1, 0)

350 **3D L-SIAC.** In three-dimensions, the basis functions are of the form

$$\chi_{S,P}^{m,r,\ell} = C \int_{-1}^1 \phi_m(\arg_x) \phi_r(\arg_y) \phi_\ell(\arg_z)$$

351 where the row of the table determines the Region (S) and Position $P = \{L, LM, RM, R\}$. The coefficient C is
352 given in the coefficient column, and the arguments of the Legendre polynomials are given in the appropriate
353 argument column. These can be found in Table 8.6. To combat the complexity of the domains of definition
354 of each filtered approximation form we introduce the classification scheme detailed in Tables 8.4 and 8.5. A
355 visual depiction of the form these regions take is given in Figure 8.1.

356 There are fifteen different forms for the coefficients included in the 3D L-SIAC case. These coefficients
357 are of the form

$$a_{R,P,m,r,\ell} = a_{m,r,\ell}(q_x, q_y, q_z) = \sum_{\gamma=-p}^p c_\gamma u_{m,r,\ell}^{i+\gamma+q_x, j+\gamma+q_y, k+\gamma+q_z},$$

358 where the coefficients (q_x, q_y, q_z) are determined by the region S and position P of the filter point. A table
359 of these dependencies by region and position is provided in Table 8.10.

Table 8.4: Regions present by octant

Octant	Regions Present
1	1A, 1B, 1C, 1D, 1E, 1F
2	2E, 2F
3	3A, 3B
4	4B, 4F
5	5C, 5D
6	6D, 6E
7	7A, 7C
8	8A, 8B, 8C, 8D, 8E, 8F

Table 8.5: Classification of regions.

Class	Filtering Coordinate Inequality
(A)	$\zeta_x \leq \zeta_y \leq \zeta_z$
(B)	$\zeta_x \leq \zeta_z < \zeta_y$
(C)	$\zeta_y < \zeta_x \leq \zeta_z$
(D)	$\zeta_y \leq \zeta_z < \zeta_x$
(E)	$\zeta_z < \zeta_y \leq \zeta_x$
(F)	$\zeta_z < \zeta_x < \zeta_y$

Table 8.6: Three-dimensional L-SIAC basis functions. For notational convenience suppose that \mathbf{x} belong to element (i, j, k) and that the region (S) and position P of the function are as indicated in the table rows.

Region (S)		Basis Function Parameters			
	Basis Function	Coefficient	\arg_x	\arg_y	\arg_z
1A	$\chi^{S,L}$	$(2 - \zeta_z)/4$	$w + \zeta_x - \zeta_z/2 - (w * \zeta_z)/2$	$w + \zeta_y - \zeta_z/2 - (w * \zeta_z)/2$	$w - ((-1 + w) * \zeta_z)/2$
1A	$\chi^{S,LM}$	$(-\zeta_y + \zeta_z)/4$	$(2 + 2 * \zeta_x - (1 + w) * \zeta_y - \zeta_z + w * \zeta_z)/2$	$(2 + \zeta_y - w * \zeta_y + (-1 + w) * \zeta_z)/2$	$(-2 - (1 + w) * \zeta_y + \zeta_z + w * \zeta_z)/2$
1A	$\chi^{S,RM}$	$(-\zeta_x + \zeta_y)/4$	$(2 + \zeta_x - w * \zeta_x + (-1 + w) * \zeta_y)/2$	$(-2 - (1 + w) * \zeta_x + \zeta_y + w * \zeta_y)/2$	$-1 - ((1 + w) * \zeta_x)/2 + ((-1 + w) * \zeta_y)/2 + \zeta_z$
1A	$\chi^{S,R}$	$\zeta_x/4$	$(-2 + \zeta_x + w * \zeta_x)/2$	$-1 + ((-1 + w) * \zeta_x)/2 + \zeta_y$	$-1 + ((-1 + w) * \zeta_x)/2 + \zeta_z$
Region	Basis Function Parameters				
1B	Basis Function	Coefficient	\arg_x	\arg_y	\arg_z
1B	$\chi^{S,L}$	$(2 - \zeta_y)/4$	$w + \zeta_x - \zeta_y/2 - (w * \zeta_y)/2$	$(-w * (-2 + \zeta_y)) + \zeta_y)/2$	$w - \zeta_y/2 - (w * \zeta_y)/2 + \zeta_z$
1B	$\chi^{S,LM}$	$(\zeta_y - \zeta_z)/4$	$(2 + 2 * \zeta_x - (1 + w) * \zeta_y - \zeta_z - w * \zeta_z)/2$	$(-2 + (1 + w) * \zeta_y - (1 + w) * \zeta_z)/2$	$(2 + (-1 + w) * \zeta_y + \zeta_z - w * \zeta_z)/2$
1B	$\chi^{S,RM}$	$(-\zeta_x + \zeta_z)/4$	$(2 + \zeta_x - w * \zeta_x + (-1 + w) * \zeta_z)/2$	$(-2 - (1 + w) * \zeta_x + 2 * \zeta_y - \zeta_z + w * \zeta_z)/2$	$(-2 - (1 + w) * \zeta_x + \zeta_z + w * \zeta_z)/2$
1B	$\chi^{S,R}$	$\zeta_x/4$	$(-2 + \zeta_x + w * \zeta_x)/2$	$-1 + ((-1 + w) * \zeta_x)/2 + \zeta_y$	$-1 + ((-1 + w) * \zeta_x)/2 + \zeta_z$
Region	Basis Function Parameters				
1C	Basis Function	Coefficient	\arg_x	\arg_y	\arg_z
1C	$\chi^{S,L}$	$(2 - \zeta_z)/4$	$w + \zeta_x - \zeta_z/2 - (w * \zeta_z)/2$	$w + \zeta_y - \zeta_z/2 - (w * \zeta_z)/2$	$w - ((-1 + w) * \zeta_z)/2$
1C	$\chi^{S,LM}$	$(-\zeta_x + \zeta_z)/4$	$(2 + \zeta_x - w * \zeta_x + (-1 + w) * \zeta_z)/2$	$(2 - (1 + w) * \zeta_x + 2 * \zeta_y - \zeta_z + w * \zeta_z)/2$	$(-2 - (1 + w) * \zeta_x + \zeta_z + w * \zeta_z)/2$
1C	$\chi^{S,RM}$	$(\zeta_x - \zeta_y)/4$	$(-2 + (1 + w) * \zeta_x - (1 + w) * \zeta_y)/2$	$(2 + (-1 + w) * \zeta_x + \zeta_y - w * \zeta_y)/2$	$-1 + ((-1 + w) * \zeta_x)/2 - ((1 + w) * \zeta_y)/2 + \zeta_z$
1C	$\chi^{S,R}$	$\zeta_y/4$	$-1 + \zeta_x + ((-1 + w) * \zeta_y)/2$	$(-2 + \zeta_y + w * \zeta_y)/2$	$-1 + ((-1 + w) * \zeta_y)/2 + \zeta_z$
Region	Basis Function Parameters				
1D	Basis Function	Coefficient	\arg_x	\arg_y	\arg_z
1D	$\chi^{S,L}$	$(2 - \zeta_x)/4$	$(-w * (-2 + \zeta_x)) + \zeta_x)/2$	$w - \zeta_x/2 - (w * \zeta_x)/2 + \zeta_y$	$w - \zeta_x/2 - (w * \zeta_x)/2 + \zeta_z$
1D	$\chi^{S,LM}$	$(\zeta_x - \zeta_z)/4$	$(-2 + (1 + w) * \zeta_x - (1 + w) * \zeta_z)/2$	$(2 + (-1 + w) * \zeta_x + 2 * \zeta_y - \zeta_z - w * \zeta_z)/2$	$(2 + (-1 + w) * \zeta_x + \zeta_z - w * \zeta_z)/2$
1D	$\chi^{S,RM}$	$(-\zeta_y + \zeta_z)/4$	$(-2 + 2 * \zeta_x - (1 + w) * \zeta_y - \zeta_z + w * \zeta_z)/2$	$(2 + \zeta_y - w * \zeta_y + (-1 + w) * \zeta_z)/2$	$(-2 - (1 + w) * \zeta_y + \zeta_z + w * \zeta_z)/2$
1D	$\chi^{S,R}$	$\zeta_y/4$	$-1 + \zeta_x + ((-1 + w) * \zeta_y)/2$	$(-2 + \zeta_y + w * \zeta_y)/2$	$-1 + ((-1 + w) * \zeta_y)/2 + \zeta_z$
Region	Basis Function Parameters				
1E	Basis Function	Coefficient	\arg_x	\arg_y	\arg_z
1E	$\chi^{S,L}$	$(2 - \zeta_x)/4$	$(-w * (-2 + \zeta_x)) + \zeta_x)/2$	$w - \zeta_x/2 - (w * \zeta_x)/2 + \zeta_y$	$w - \zeta_x/2 - (w * \zeta_x)/2 + \zeta_z$
1E	$\chi^{S,LM}$	$(\zeta_x - \zeta_y)/4$	$(-2 + (1 + w) * \zeta_x - (1 + w) * \zeta_y)/2$	$(2 + (-1 + w) * \zeta_x + \zeta_y - w * \zeta_y)/2$	$1 + ((-1 + w) * \zeta_x)/2 - ((1 + w) * \zeta_y)/2 + \zeta_z$
1E	$\chi^{S,RM}$	$(\zeta_y - \zeta_z)/4$	$(-2 + 2 * \zeta_x + (-1 + w) * \zeta_y - \zeta_z - w * \zeta_z)/2$	$(-2 + (1 + w) * \zeta_y - (1 + w) * \zeta_z)/2$	$(2 + (-1 + w) * \zeta_y + \zeta_z - w * \zeta_z)/2$
1E	$\chi^{S,R}$	$\zeta_z/4$	$-1 + \zeta_x + ((-1 + w) * \zeta_z)/2$	$-1 + \zeta_y + ((-1 + w) * \zeta_z)/2$	$(-2 + \zeta_z + w * \zeta_z)/2$
Region	Basis Function Parameters				
1F	Basis Function	Coefficient	\arg_x	\arg_y	\arg_z
1F	$\chi^{S,L}$	$(2 - \zeta_y)/4$	$w + \zeta_x - \zeta_y/2 - (w * \zeta_y)/2$	$(-w * (-2 + \zeta_y)) + \zeta_y)/2$	$w - \zeta_y/2 - (w * \zeta_y)/2 + \zeta_z$
1F	$\chi^{S,LM}$	$(-\zeta_x + \zeta_y)/4$	$(2 + \zeta_x - w * \zeta_x + (-1 + w) * \zeta_y)/2$	$(-2 - (1 + w) * \zeta_x + \zeta_y + w * \zeta_y)/2$	$1 - ((1 + w) * \zeta_x)/2 + ((-1 + w) * \zeta_y)/2 + \zeta_z$
1F	$\chi^{S,RM}$	$(\zeta_x - \zeta_z)/4$	$(-2 + (1 + w) * \zeta_x - (1 + w) * \zeta_z)/2$	$(-2 + (-1 + w) * \zeta_x + 2 * \zeta_y - \zeta_z - w * \zeta_z)/2$	$(2 + (-1 + w) * \zeta_x + \zeta_z - w * \zeta_z)/2$
1F	$\chi^{S,R}$	$\zeta_z/4$	$-1 + \zeta_x + ((-1 + w) * \zeta_z)/2$	$-1 + \zeta_y + ((-1 + w) * \zeta_z)/2$	$(-2 + \zeta_z + w * \zeta_z)/2$

Table 8.6 cont.

Region		Basis Function Parameters					
	Basis Function	Coefficient	\arg_x	\arg_y	\arg_z		
2E	$\chi^{S,L}$	$-\zeta_z/4$	$-1 + \zeta_x - ((1+w)*\zeta_z)/2$	$-1 + \zeta_y - ((1+w)*\zeta_z)/2$	$(2 + \zeta_z - w*\zeta_z)/2$		
2E	$\chi^{S,LM}$	$(2 - \zeta_x + \zeta_z)/4$	$(\zeta_x - \zeta_z + w*(2 - \zeta_x + \zeta_z))/2$	$(-\zeta_x + 2*\zeta_y - \zeta_z + w*(2 - \zeta_x + \zeta_z))/2$	$(-\zeta_x + \zeta_z + w*(2 - \zeta_x + \zeta_z))/2$		
2E	$\chi^{S,RM}$	$(\zeta_x - \zeta_y)/4$	$(-2 + (1+w)*\zeta_x - (1+w)*\zeta_y)/2$	$(2 + (-1+w)*\zeta_x + \zeta_y - w*\zeta_y)/2$	$1 + ((-1+w)*\zeta_x)/2 - ((1+w)*\zeta_y)/2 + \zeta_z$		
2E	$\chi^{S,R}$	$\zeta_y/4$	$-1 + \zeta_x + ((-1+w)*\zeta_y)/2$	$(-2 + \zeta_y + w*\zeta_y)/2$	$1 + ((-1+w)*\zeta_y)/2 + \zeta_z$		
Region		Basis Function Parameters					
	Basis Function	Coefficient	\arg_x	\arg_y	\arg_z		
2F	$\chi^{S,L}$	$-\zeta_z/4$	$-1 + \zeta_x - ((1+w)*\zeta_z)/2$	$-1 + \zeta_y - ((1+w)*\zeta_z)/2$	$(2 + \zeta_z - w*\zeta_z)/2$		
2F	$\chi^{S,LM}$	$(2 - \zeta_y + \zeta_z)/4$	$(2*\zeta_x - \zeta_y - \zeta_z + w*(2 - \zeta_y + \zeta_z))/2$	$(\zeta_y - \zeta_z + w*(2 - \zeta_y + \zeta_z))/2$	$(-\zeta_y + \zeta_z + w*(2 - \zeta_y + \zeta_z))/2$		
2F	$\chi^{S,RM}$	$(-\zeta_x + \zeta_y)/4$	$(2 + \zeta_x - w*\zeta_x + (-1+w)*\zeta_y)/2$	$(-2 - (1+w)*\zeta_x + \zeta_y + w*\zeta_y)/2$	$1 - ((1+w)*\zeta_x)/2 + ((-1+w)*\zeta_y)/2 + \zeta_z$		
2F	$\chi^{S,R}$	$\zeta_x/4$	$(-2 + \zeta_x + w*\zeta_x)/2$	$-1 + ((-1+w)*\zeta_x)/2 + \zeta_y$	$1 + ((-1+w)*\zeta_x)/2 + \zeta_z$		
Region		Basis Function Parameters					
	Basis Function	Coefficient	\arg_x	\arg_y	\arg_z		
3A	$\chi^{S,L}$	$-\zeta_x/4$	$(2 + \zeta_x - w*\zeta_x)/2$	$-1 - ((1+w)*\zeta_x)/2 + \zeta_y$	$-1 - ((1+w)*\zeta_x)/2 + \zeta_z$		
3A	$\chi^{S,LM}$	$(2 + \zeta_x - \zeta_z)/4$	$(\zeta_x + w*(2 + \zeta_x - \zeta_z) - \zeta_z)/2$	$(-\zeta_x + 2*\zeta_y + w*(2 + \zeta_x - \zeta_z) - \zeta_z)/2$	$(-\zeta_x + w*(2 + \zeta_x - \zeta_z) + \zeta_z)/2$		
3A	$\chi^{S,RM}$	$(-\zeta_y + \zeta_z)/4$	$(2 + 2*\zeta_x - (1+w)*\zeta_y - \zeta_z + w*\zeta_z)/2$	$(2 + \zeta_y - w*\zeta_y + (-1+w)*\zeta_z)/2$	$(-2 - (1+w)*\zeta_y + \zeta_z + w*\zeta_z)/2$		
3A	$\chi^{S,R}$	$\zeta_y/4$	$1 + \zeta_x + ((-1+w)*\zeta_y)/2$	$(-2 + \zeta_y + w*\zeta_y)/2$	$-1 + ((-1+w)*\zeta_y)/2 + \zeta_z$		
Region		Basis Function Parameters					
	Basis Function	Coefficient	\arg_x	\arg_y	\arg_z		
3B	$\chi^{S,L}$	$-\zeta_x/4$	$(2 + \zeta_x - w*\zeta_x)/2$	$-1 - ((1+w)*\zeta_x)/2 + \zeta_y$	$-1 - ((1+w)*\zeta_x)/2 + \zeta_z$		
3B	$\chi^{S,LM}$	$(2 + \zeta_x - \zeta_y)/4$	$(\zeta_x + w*(2 + \zeta_x - \zeta_y) - \zeta_y)/2$	$(-\zeta_x + w*(2 + \zeta_x - \zeta_y) + \zeta_y)/2$	$(-\zeta_x + w*(2 + \zeta_x - \zeta_y) - \zeta_y + 2*\zeta_z)/2$		
3B	$\chi^{S,RM}$	$(\zeta_y - \zeta_z)/4$	$(2 + 2*\zeta_x + (-1+w)*\zeta_y - \zeta_z - w*\zeta_z)/2$	$(-2 + (1+w)*\zeta_y - (1+w)*\zeta_z)/2$	$(2 + (-1+w)*\zeta_y + \zeta_z - w*\zeta_z)/2$		
3B	$\chi^{S,R}$	$\zeta_z/4$	$1 + \zeta_x + ((-1+w)*\zeta_z)/2$	$-1 + \zeta_y + ((-1+w)*\zeta_z)/2$	$(-2 + \zeta_z + w*\zeta_z)/2$		
Region		Basis Function Parameters					
	Basis Function	Coefficient	\arg_x	\arg_y	\arg_z		
4B	$\chi^{S,L}$	$-\zeta_z/4$	$1 + \zeta_x - ((1+w)*\zeta_z)/2$	$-1 + \zeta_y - ((1+w)*\zeta_z)/2$	$(2 + \zeta_z - w*\zeta_z)/2$		
4B	$\chi^{S,LM}$	$(-\zeta_x + \zeta_z)/4$	$(2 + \zeta_x - w*\zeta_x + (-1+w)*\zeta_z)/2$	$(-2 - (1+w)*\zeta_x + 2*\zeta_y - \zeta_z + w*\zeta_z)/2$	$(-2 - (1+w)*\zeta_x + \zeta_z + w*\zeta_z)/2$		
4B	$\chi^{S,RM}$	$(2 + \zeta_x - \zeta_y)/4$	$(\zeta_x + w*(2 + \zeta_x - \zeta_y) - \zeta_y)/2$	$(-\zeta_x + w*(2 + \zeta_x - \zeta_y) + \zeta_y)/2$	$(-\zeta_x + w*(2 + \zeta_x - \zeta_y) - \zeta_y + 2*\zeta_z)/2$		
4B	$\chi^{S,R}$	$\zeta_y/4$	$1 + \zeta_x + ((-1+w)*\zeta_y)/2$	$(-2 + \zeta_y + w*\zeta_y)/2$	$1 + ((-1+w)*\zeta_y)/2 + \zeta_z$		
Region		Basis Function Parameters					
	Basis Function	Coefficient	\arg_x	\arg_y	\arg_z		
4F	$\chi^{S,L}$	$-\zeta_x/4$	$(2 + \zeta_x - w*\zeta_x)/2$	$-1 - ((1+w)*\zeta_x)/2 + \zeta_y$	$1 - ((1+w)*\zeta_x)/2 + \zeta_z$		
4F	$\chi^{S,LM}$	$(\zeta_x - \zeta_z)/4$	$(-2 + (1+w)*\zeta_x - (1+w)*\zeta_z)/2$	$(-2 + (-1+w)*\zeta_x + 2*\zeta_y - \zeta_z - w*\zeta_z)/2$	$(2 + (-1+w)*\zeta_x + \zeta_z - w*\zeta_z)/2$		
4F	$\chi^{S,RM}$	$(2 - \zeta_y + \zeta_z)/4$	$(2*\zeta_x - \zeta_y - \zeta_z + w*(2 - \zeta_y + \zeta_z))/2$	$(\zeta_y - \zeta_z + w*(2 - \zeta_y + \zeta_z))/2$	$(-\zeta_y + \zeta_z + w*(2 - \zeta_y + \zeta_z))/2$		
4F	$\chi^{S,R}$	$\zeta_y/4$	$1 + \zeta_x + ((-1+w)*\zeta_y)/2$	$(-2 + \zeta_y + w*\zeta_y)/2$	$1 + ((-1+w)*\zeta_y)/2 + \zeta_z$		

Table 8.6 cont.

Basis Function Parameters					
Region	Basis Function	Coefficient	\arg_x	\arg_y	\arg_z
5C	$\chi^{S,L}$	$-\zeta_y/4$	$-1 + \zeta_x - ((1+w)*\zeta_y)/2$	$(2 + \zeta_y - w*\zeta_y)/2$	$-1 - ((1+w)*\zeta_y)/2 + \zeta_z$
5C	$\chi^{S,LM}$	$(2 + \zeta_y - \zeta_z)/4$	$(2 * \zeta_x - \zeta_y + w * (2 + \zeta_y - \zeta_z) - \zeta_z)/2$	$(\zeta_y + w * (2 + \zeta_y - \zeta_z) - \zeta_z)/2$	$(-\zeta_y + w * (2 + \zeta_y - \zeta_z) + \zeta_z)/2$
5C	$\chi^{S,RM}$	$(-\zeta_x + \zeta_z)/4$	$(2 + \zeta_x - w * \zeta_x + (-1+w)*\zeta_z)/2$	$(2 - (1+w)*\zeta_x + 2*\zeta_y - \zeta_z + w*\zeta_z)/2$	$(-2 - (1+w)*\zeta_x + \zeta_z + w*\zeta_z)/2$
5C	$\chi^{S,R}$	$\zeta_x/4$	$(-2 + \zeta_x + w * \zeta_x)/2$	$1 + ((-1+w)*\zeta_x)/2 + \zeta_y$	$-1 + ((-1+w)*\zeta_x)/2 + \zeta_z$
Basis Function Parameters					
Region	Basis Function	Coefficient	\arg_x	\arg_y	\arg_z
5D	$\chi^{S,L}$	$-\zeta_y/4$	$-1 + \zeta_x - ((1+w)*\zeta_y)/2$	$(2 + \zeta_y - w*\zeta_y)/2$	$-1 - ((1+w)*\zeta_y)/2 + \zeta_z$
5D	$\chi^{S,LM}$	$(2 - \zeta_x + \zeta_y)/4$	$(\zeta_x - \zeta_y + w * (2 - \zeta_x + \zeta_y))/2$	$(-\zeta_x + \zeta_y + w * (2 - \zeta_x + \zeta_y))/2$	$(-\zeta_x - \zeta_y + w * (2 - \zeta_x + \zeta_y) + 2 * \zeta_z)/2$
5D	$\chi^{S,RM}$	$(\zeta_x - \zeta_z)/4$	$(-2 + (1+w)*\zeta_x - (1+w)*\zeta_z)/2$	$(2 + (-1+w)*\zeta_x + 2*\zeta_y - \zeta_z - w*\zeta_z)/2$	$(2 + (-1+w)*\zeta_x + \zeta_z - w*\zeta_z)/2$
5D	$\chi^{S,R}$	$\zeta_z/4$	$-1 + \zeta_x + ((-1+w)*\zeta_z)/2$	$1 + \zeta_y + ((-1+w)*\zeta_z)/2$	$(-2 + \zeta_z + w * \zeta_z)/2$
Basis Function Parameters					
Region	Basis Function	Coefficient	\arg_x	\arg_y	\arg_z
6D	$\chi^{S,L}$	$-\zeta_z/4$	$-1 + \zeta_x - ((1+w)*\zeta_z)/2$	$1 + \zeta_y - ((1+w)*\zeta_z)/2$	$(2 + \zeta_z - w * \zeta_z)/2$
6D	$\chi^{S,LM}$	$(-\zeta_y + \zeta_z)/4$	$(-2 + 2 * \zeta_x - (1+w)*\zeta_y - \zeta_z + w * \zeta_z)/2$	$(2 + \zeta_y - w * \zeta_y + (-1+w)*\zeta_z)/2$	$(-2 - (1+w)*\zeta_y + \zeta_z + w * \zeta_z)/2$
6D	$\chi^{S,RM}$	$(2 - \zeta_x + \zeta_y)/4$	$(\zeta_x - \zeta_y + w * (2 - \zeta_x + \zeta_y))/2$	$(-\zeta_x + \zeta_y + w * (2 - \zeta_x + \zeta_y))/2$	$(-\zeta_x - \zeta_y + w * (2 - \zeta_x + \zeta_y) + 2 * \zeta_z)/2$
6D	$\chi^{S,R}$	$\zeta_x/4$	$(-2 + \zeta_x + w * \zeta_x)/2$	$1 + ((-1+w)*\zeta_x)/2 + \zeta_y$	$1 + ((-1+w)*\zeta_x)/2 + \zeta_z$
Basis Function Parameters					
Region	Basis Function	Coefficient	\arg_x	\arg_y	\arg_z
6E	$\chi^{S,L}$	$-\zeta_y/4$	$-1 + \zeta_x - ((1+w)*\zeta_y)/2$	$(2 + \zeta_y - w * \zeta_y)/2$	$1 - ((1+w)*\zeta_y)/2 + \zeta_z$
6E	$\chi^{S,LM}$	$(\zeta_y - \zeta_z)/4$	$(-2 + 2 * \zeta_x + (-1+w)*\zeta_y - \zeta_z - w * \zeta_z)/2$	$(-2 + (1+w)*\zeta_y - (1+w)*\zeta_z)/2$	$(2 + (-1+w)*\zeta_y + \zeta_z - w * \zeta_z)/2$
6E	$\chi^{S,RM}$	$(2 - \zeta_x + \zeta_z)/4$	$(\zeta_x - \zeta_z + w * (2 - \zeta_x + \zeta_z))/2$	$(-\zeta_x + 2 * \zeta_y - \zeta_z + w * (2 - \zeta_x + \zeta_z))/2$	$(-\zeta_x + \zeta_z + w * (2 - \zeta_x + \zeta_z))/2$
6E	$\chi^{S,R}$	$\zeta_x/4$	$(-2 + \zeta_x + w * \zeta_x)/2$	$1 + ((-1+w)*\zeta_x)/2 + \zeta_y$	$1 + ((-1+w)*\zeta_x)/2 + \zeta_z$
Basis Function Parameters					
Region	Basis Function	Coefficient	\arg_x	\arg_y	\arg_z
7A	$\chi^{S,L}$	$-\zeta_y/4$	$1 + \zeta_x - ((1+w)*\zeta_y)/2$	$(2 + \zeta_y - w * \zeta_y)/2$	$-1 - ((1+w)*\zeta_y)/2 + \zeta_z$
7A	$\chi^{S,LM}$	$(-\zeta_x + \zeta_y)/4$	$(2 + \zeta_x - w * \zeta_x + (-1+w)*\zeta_y)/2$	$(-2 - (1+w)*\zeta_x + \zeta_y + w * \zeta_y)/2$	$-1 - ((1+w)*\zeta_x)/2 + ((-1+w)*\zeta_y)/2 + \zeta_z$
7A	$\chi^{S,RM}$	$(2 + \zeta_x - \zeta_z)/4$	$(\zeta_x + w * (2 + \zeta_x - \zeta_z) - \zeta_z)/2$	$(-\zeta_x + 2 * \zeta_y + w * (2 + \zeta_x - \zeta_z) - \zeta_z)/2$	$(-\zeta_x + w * (2 + \zeta_x - \zeta_z) + \zeta_z)/2$
7A	$\chi^{S,R}$	$\zeta_z/4$	$1 + \zeta_x + ((-1+w)*\zeta_z)/2$	$1 + \zeta_y + ((-1+w)*\zeta_z)/2$	$(-2 + \zeta_z + w * \zeta_z)/2$
Basis Function Parameters					
Region	Basis Function	Coefficient	\arg_x	\arg_y	\arg_z
7C	$\chi^{S,L}$	$-\zeta_x/4$	$(2 + \zeta_x - w * \zeta_x)/2$	$1 - ((1+w)*\zeta_x)/2 + \zeta_y$	$-1 - ((1+w)*\zeta_x)/2 + \zeta_z$
7C	$\chi^{S,LM}$	$(\zeta_x - \zeta_y)/4$	$(-2 + (1+w)*\zeta_x - (1+w)*\zeta_y)/2$	$(2 + (-1+w)*\zeta_x + \zeta_y - w * \zeta_y)/2$	$-1 + ((-1+w)*\zeta_x)/2 - ((1+w)*\zeta_y)/2 + \zeta_z$
7C	$\chi^{S,RM}$	$(2 + \zeta_y - \zeta_z)/4$	$(2 * \zeta_x - \zeta_y + w * (2 + \zeta_y - \zeta_z) - \zeta_z)/2$	$(\zeta_y + w * (2 + \zeta_y - \zeta_z) - \zeta_z)/2$	$(-\zeta_y + w * (2 + \zeta_y - \zeta_z) + \zeta_z)/2$
7C	$\chi^{S,R}$	$\zeta_z/4$	$1 + \zeta_x + ((-1+w)*\zeta_z)/2$	$1 + \zeta_y + ((-1+w)*\zeta_z)/2$	$(-2 + \zeta_z + w * \zeta_z)/2$

Table 8.6 cont.

Basis Function Parameters					
Region	Basis Function	Coefficient	\arg_x	\arg_y	\arg_z
8A	$\chi^{S,L}$	$-\zeta_z/4$	$1 + \zeta_x - ((1+w)*\zeta_z)/2$	$1 + \zeta_y - ((1+w)*\zeta_z)/2$	$(2 + \zeta_z - w*\zeta_z)/2$
8A	$\chi^{S,LM}$	$(-\zeta_y + \zeta_z)/4$	$(2 + 2*\zeta_x - (1+w)*\zeta_y - \zeta_z + w*\zeta_z)/2$	$(2 + \zeta_y - w*\zeta_y + (-1+w)*\zeta_z)/2$	$(-2 - (1+w)*\zeta_y + \zeta_z + w*\zeta_z)/2$
8A	$\chi^{S,RM}$	$(-\zeta_x + \zeta_y)/4$	$(2 + \zeta_x - w*\zeta_x + (-1+w)*\zeta_y)/2$	$(-2 - (1+w)*\zeta_x + \zeta_y + w*\zeta_y)/2$	$-1 - ((1+w)*\zeta_x)/2 + ((-1+w)*\zeta_y)/2 + \zeta_z$
8A	$\chi^{S,R}$	$(2 + \zeta_x)/4$	$(\zeta_x + w*(2 + \zeta_x))/2$	$w - \zeta_x/2 + (w*\zeta_x)/2 + \zeta_y$	$w - \zeta_x/2 + (w*\zeta_x)/2 + \zeta_z$
Basis Function Parameters					
Region	Basis Function	Coefficient	\arg_x	\arg_y	\arg_z
8B	$\chi^{S,L}$	$-\zeta_y/4$	$1 + \zeta_x - ((1+w)*\zeta_y)/2$	$(2 + \zeta_y - w*\zeta_y)/2$	$1 - ((1+w)*\zeta_y)/2 + \zeta_z$
8B	$\chi^{S,LM}$	$(\zeta_y - \zeta_z)/4$	$(2 + 2*\zeta_x - (1+w)*\zeta_y - \zeta_z - w*\zeta_z)/2$	$(-2 + (1+w)*\zeta_y - (1+w)*\zeta_z)/2$	$(2 + (-1+w)*\zeta_y + \zeta_z - w*\zeta_z)/2$
8B	$\chi^{S,RM}$	$(-\zeta_x + \zeta_z)/4$	$(2 + \zeta_x - w*\zeta_x + (-1+w)*\zeta_z)/2$	$(-2 - (1+w)*\zeta_x + 2*\zeta_y - \zeta_z + w*\zeta_z)/2$	$(-2 - (1+w)*\zeta_x + \zeta_z + w*\zeta_z)/2$
8B	$\chi^{S,R}$	$(2 + \zeta_x)/4$	$(\zeta_x + w*(2 + \zeta_x))/2$	$w - \zeta_x/2 + (w*\zeta_x)/2 + \zeta_y$	$w - \zeta_x/2 + (w*\zeta_x)/2 + \zeta_z$
Basis Function Parameters					
Region	Basis Function	Coefficient	\arg_x	\arg_y	\arg_z
8C	$\chi^{S,L}$	$-\zeta_z/4$	$1 + \zeta_x - ((1+w)*\zeta_z)/2$	$1 + \zeta_y - ((1+w)*\zeta_z)/2$	$(2 + \zeta_z - w*\zeta_z)/2$
8C	$\chi^{S,LM}$	$(-\zeta_x + \zeta_z)/4$	$(2 + \zeta_x - w*\zeta_x + (-1+w)*\zeta_z)/2$	$(2 - (1+w)*\zeta_x + 2*\zeta_y - \zeta_z + w*\zeta_z)/2$	$(-2 - (1+w)*\zeta_x + \zeta_z + w*\zeta_z)/2$
8C	$\chi^{S,RM}$	$(\zeta_x - \zeta_y)/4$	$(-2 + (1+w)*\zeta_x - (1+w)*\zeta_y)/2$	$(2 + (-1+w)*\zeta_x + \zeta_y - w*\zeta_y)/2$	$-1 + ((-1+w)*\zeta_x)/2 - ((1+w)*\zeta_y)/2 + \zeta_z$
8C	$\chi^{S,R}$	$(2 + \zeta_y)/4$	$w + \zeta_x - \zeta_y/2 + (w*\zeta_y)/2$	$(\zeta_y + w*(2 + \zeta_y))/2$	$w - \zeta_y/2 + (w*\zeta_y)/2 + \zeta_z$
Basis Function Parameters					
Region	Basis Function	Coefficient	\arg_x	\arg_y	\arg_z
8D	$\chi^{S,L}$	$-\zeta_x/4$	$(2 + \zeta_x - w*\zeta_x)/2$	$1 - ((1+w)*\zeta_x)/2 + \zeta_y$	$1 - ((1+w)*\zeta_x)/2 + \zeta_z$
8D	$\chi^{S,LM}$	$(\zeta_x - \zeta_z)/4$	$(-2 + (1+w)*\zeta_x - (1+w)*\zeta_z)/2$	$(2 + (-1+w)*\zeta_x + 2*\zeta_y - \zeta_z - w*\zeta_z)/2$	$(2 + (-1+w)*\zeta_x + \zeta_z - w*\zeta_z)/2$
8D	$\chi^{S,RM}$	$(-\zeta_y + \zeta_z)/4$	$(-2 + 2*\zeta_x - (1+w)*\zeta_y - \zeta_z + w*\zeta_z)/2$	$(2 + \zeta_y - w*\zeta_y + (-1+w)*\zeta_z)/2$	$(-2 - (1+w)*\zeta_y + \zeta_z + w*\zeta_z)/2$
8D	$\chi^{S,R}$	$(2 + \zeta_y)/4$	$w + \zeta_x - \zeta_y/2 + (w*\zeta_y)/2$	$(\zeta_y + w*(2 + \zeta_y))/2$	$w - \zeta_y/2 + (w*\zeta_y)/2 + \zeta_z$
Basis Function Parameters					
Region	Basis Function	Coefficient	\arg_x	\arg_y	\arg_z
8E	$\chi^{S,L}$	$-\zeta_x/4$	$(2 + \zeta_x - w*\zeta_x)/2$	$1 - ((1+w)*\zeta_x)/2 + \zeta_y$	$1 - ((1+w)*\zeta_x)/2 + \zeta_z$
8E	$\chi^{S,LM}$	$(\zeta_x - \zeta_y)/4$	$(-2 + (1+w)*\zeta_x - (1+w)*\zeta_y)/2$	$(2 + (-1+w)*\zeta_x + \zeta_y - w*\zeta_y)/2$	$1 + ((-1+w)*\zeta_x)/2 - ((1+w)*\zeta_y)/2 + \zeta_z$
8E	$\chi^{S,RM}$	$(\zeta_y - \zeta_z)/4$	$(-2 + 2*\zeta_x - (-1+w)*\zeta_y - \zeta_z - w*\zeta_z)/2$	$(-2 + (1+w)*\zeta_y - (1+w)*\zeta_z)/2$	$(2 + (-1+w)*\zeta_y + \zeta_z - w*\zeta_z)/2$
8E	$\chi^{S,R}$	$(2 + \zeta_z)/4$	$w + \zeta_x - \zeta_z/2 + (w*\zeta_z)/2$	$w + \zeta_y - \zeta_z/2 + (w*\zeta_z)/2$	$w + ((1+w)*\zeta_z)/2$
Basis Function Parameters					
Region	Basis Function	Coefficient	\arg_x	\arg_y	\arg_z
8F	$\chi^{S,L}$	$-\zeta_y/4$	$1 + \zeta_x - ((1+w)*\zeta_y)/2$	$(2 + \zeta_y - w*\zeta_y)/2$	$1 - ((1+w)*\zeta_y)/2 + \zeta_z$
8F	$\chi^{S,LM}$	$(-\zeta_x + \zeta_y)/4$	$(2 + \zeta_x - w*\zeta_x + (-1+w)*\zeta_y)/2$	$(-2 - (1+w)*\zeta_x + \zeta_y + w*\zeta_y)/2$	$1 - ((1+w)*\zeta_x)/2 + ((-1+w)*\zeta_y)/2 + \zeta_z$
8F	$\chi^{S,RM}$	$(\zeta_x - \zeta_z)/4$	$(-2 + (1+w)*\zeta_x - (1+w)*\zeta_z)/2$	$(-2 + (-1+w)*\zeta_x + 2*\zeta_y - \zeta_z - w*\zeta_z)/2$	$(2 + (-1+w)*\zeta_x + \zeta_z - w*\zeta_z)/2$
8F	$\chi^{S,R}$	$(2 + \zeta_z)/4$	$w + \zeta_x - \zeta_z/2 + (w*\zeta_z)/2$	$w + \zeta_y - \zeta_z/2 + (w*\zeta_z)/2$	$w + ((1+w)*\zeta_z)/2$

Table 8.10: Table describing how the shifting arguments (q_x, q_y, q_z) of the a coefficients vary by region.

Region (S) \ Arguments of $a_\alpha(q_x, q_y, q_z)$	$P = L$	$P = LM$	$P = RM$	$P = R$
1A	(0, 0, 0)	(0, 0, 1)	(0, 1, 1)	(1, 1, 1)
1B	(0, 0, 0)	(0, 1, 0)	(0, 1, 1)	(1, 1, 1)
1C	(0, 0, 0)	(0, 0, 1)	(1, 0, 1)	(1, 1, 1)
1D	(0, 0, 0)	(1, 0, 0)	(1, 0, 1)	(1, 1, 1)
1E	(0, 0, 0)	(1, 0, 0)	(1, 1, 0)	(1, 1, 1)
1F	(0, 0, 0)	(0, 1, 0)	(1, 1, 0)	(1, 1, 1)
2E	(0, 0, -1)	(0, 0, 0)	(1, 0, 0)	(1, 1, 0)
2F	(0, 0, -1)	(0, 0, 0)	(0, 1, 0)	(1, 1, 0)
3A	(-1, 0, 0)	(0, 0, 0)	(0, 0, 1)	(0, 1, 1)
3B	(-1, 0, 0)	(0, 0, 0)	(0, 1, 0)	(0, 1, 1)
4B	(-1, 0, -1)	(-1, 0, 0)	(0, 0, 0)	(0, 1, 0)
4F	(-1, 0, -1)	(0, 0, -1)	(0, 0, 0)	(0, 1, 0)
5C	(0, -1, 0)	(0, 0, 0)	(0, 0, 1)	(1, 0, 1)
5D	(0, -1, 0)	(0, 0, 0)	(1, 0, 0)	(1, 0, 1)
6D	(0, -1, -1)	(0, -1, 0)	(0, 0, 0)	(1, 0, 0)
6E	(0, -1, -1)	(0, 0, -1)	(0, 0, 0)	(1, 0, 0)
7A	(-1, -1, 0)	(-1, 0, 0)	(0, 0, 0)	(0, 0, 1)
7C	(-1, -1, 0)	(0, -1, 0)	(0, 0, 0)	(0, 0, 1)
8A	(-1, -1, -1)	(-1, -1, 0)	(-1, 0, 0)	(0, 0, 0)
8B	(-1, -1, -1)	(-1, 0, -1)	(-1, 0, 0)	(0, 0, 0)
8C	(-1, -1, -1)	(-1, -1, 0)	(0, -1, 0)	(0, 0, 0)
8D	(-1, -1, -1)	(0, -1, -1)	(0, -1, 0)	(0, 0, 0)
8E	(-1, -1, -1)	(0, -1, -1)	(0, 0, -1)	(0, 0, 0)
8F	(-1, -1, -1)	(-1, 0, -1)	(0, 0, -1)	(0, 0, 0)

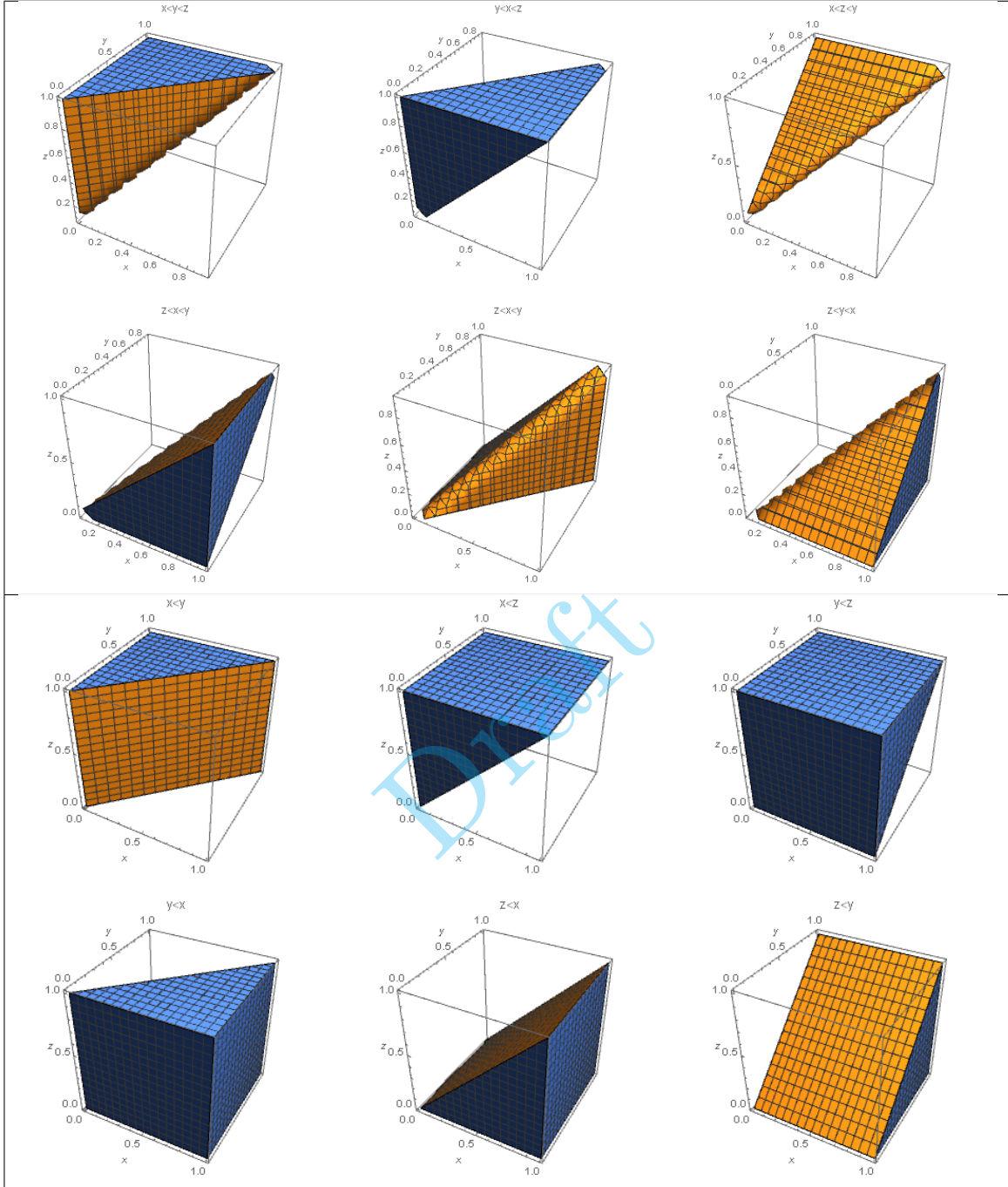


Fig. 8.1: Depiction of how the domain of dependence of the filtered approximation form varies from octant to octant. Octants 1 and 8 have six regions each (Top), while octants 2 through 7 have only a pair of regions each (Bottom). The form of these regions are a result of the filtering coordinate inequalities given in Table 8.5 coupled with the relative location of each octant in the reference element.